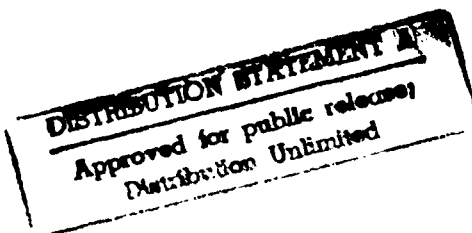
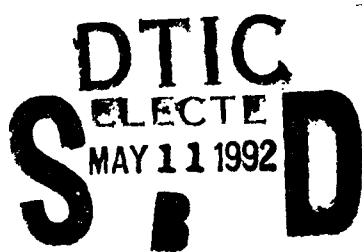




Form Approved
OMB No. 0704-0183

Average 1-hour on-response, using the same for reviewing instructor's year-end, existing data, allowing the direction of information. Send comments regarding this burden estimate or any other aspect of this collection of information, including suggestions for reducing this burden, to Washington Headquarters Services, Directorate for Information Operations and Reports, 1215 Jefferson Avenue, Washington, DC 20503.

1. AGENCY USE ONLY (Leave blank)		2. REPORT DATE 1991		3. REPORT TYPE AND DATES COVERED THESIS/DOSSIERATION	
4. TITLE AND SUBTITLE Tropical Cyclone Asymmetries As Revealed by Recent Satellite Microwave Brightness Temperatures				5. FUNDING NUMBERS	
6. AUTHOR(S) Jeffrey H. McCoy, Capt					
7. PERFORMING ORGANIZATION NAME(S) AND ADDRESS(ES) AFIT Student Attending: St. Louis University				8. PERFORMING ORGANIZATION REPORT NUMBER AFIT/CI/CIA- 91-117	
9. SPONSORING / MONITORING AGENCY NAME(S) AND ADDRESS(ES) AFIT/CI Wright-Patterson AFB OH 45433-6583				10. SPONSORING / MONITORING AGENCY REPORT NUMBER	
11. SUPPLEMENTARY NOTES					
12a. DISTRIBUTION / AVAILABILITY STATEMENT Approved for Public Release IAW 190-1 Distributed Unlimited ERNEST A. HAYGOOD, Captain, USAF Executive Officer				12b. DISTRIBUTION CODE	
13. ABSTRACT (Maximum 200 words)					
<div style="float: left; width: 30%;">  </div> <div style="float: right; width: 60%; text-align: center;">  </div>					
14. SUBJECT TERMS				15. NUMBER OF PAGES 133	
				16. PRICE CODE	
17. SECURITY CLASSIFICATION OF REPORT		18. SECURITY CLASSIFICATION OF THIS PAGE		19. SECURITY CLASSIFICATION OF ABSTRACT	
				20. LIMITATION OF ABSTRACT	

**TROPICAL CYCLONE ASYMMETRIES AS REVEALED BY RECENT
SATELLITE MICROWAVE BRIGHTNESS TEMPERATURES**

Jeffrey Hale McCoy, B.S.

A Digest Presented to the Faculty of the Graduate
School of Saint Louis University in Partial
Fulfillment of the Requirements for the
Degree of Master of Science (Research)

1991

92-11988



92 5 01 036

**TROPICAL CYCLONE ASYMMETRIES AS REVEALED BY RECENT
SATELLITE MICROWAVE BRIGHTNESS TEMPERATURES**

Jeffrey Hale McCoy, B.S.

A Thesis Presented to the Faculty of the Graduate
School of Saint Louis University in Partial
Fulfillment of the Requirements for the
Degree of Master of Science (Research)

1991

COMMITTEE IN CHARGE OF CANDIDACY:

Professor Gandikota V. Rao,
Chairman and Advisor

Assistant Professor Lawrence Coy

Associate Professor James T. Moore

This thesis is dedicated to
the memory of my father,
Richard E. McCoy

ACKNOWLEDGMENTS

I would like to thank several people who have offered their assistance during the preparation of this thesis. Prof. Gandikota V. Rao, my graduate advisor, provided valuable guidance and support and was instrumental in the successful completion of this research. Mr. Gerald Felde at the Air Force Geophysics Laboratory kindly provided the necessary data and software from which this research was based. I would also like to thank Prof. Lawrence Coy, Prof. James T. Moore, and Capt. Paul (Doug) Mac Arthur for their much appreciated comments and suggestions. Mr. Mark Baricevic at the St. Louis University Computer Center offered his time and computer expertise. Also, Mr. Frank Wells, at the Joint Typhoon and Warning Center, provided typhoon track and fix data. The photos were reproduced by the Air Force photo lab at Scott AFB, IL. My master's program was sponsored by the Air Force Institute of Technology. Finally, I would like to thank my wife, Tina, whose support, tolerance, and inspiration led to the successful completion of my master's program.

TABLE OF CONTENTS

	Page
Chapter I. Introduction.....	1
Chapter II. Review of Related Literature.....	5
Chapter III. The Microwave Imager and Data	
a. The Special Sensor Microwave Imager.....	15
b. The data.....	19
c. Microwave radiative transfer properties.....	23
Chapter IV. The Procedure/Methodology	
a. Data collection.....	34
b. Calculation of statistics.....	37
c. Brightness temperature anomalies.....	41
d. Analysis.....	44
Chapter V. The Results	
a. General.....	49
b. Mean Brightness Temperatures..	50
c. Brightness Temperature anomalies.....	64
d. Lynn: a case study.....	94
Chapter VI. Conclusions.....	123
Appendix. Definition of terms.....	126
References.....	128
Biography of the author.....	133

LIST OF TABLES

	Page
Table 4.1. SSM/I map times of typhoons and one tropical cyclone (04B) used in this study...	36
Table 4.2. Variations in box radii (km) used in this study to generate anomalies and conduct statistical analyses.....	47
Table 5.1. Cyclone map times with ice hydrometeors as determined by Spencer and Hood (1989) methodology (Fig. 5.5).....	57
Table 5.2. Typhoon Lynn's lifecycle data.....	95

LIST OF ILLUSTRATIONS

	Page
Fig. 2.1. Two aircraft flight legs of TB measurements over a thunderstorm complex. Various microwave frequencies and one IR frequency, 11 micrometers, are shown (after Adler et al., 1990).....	9
Fig. 3.1. SSM/I scan geometry. The satellite travels in the direction marked "subtrack" while the SSM/I instrument rotates around the axis labeled "x" (after Hollinger et al., 1987).....	16
Fig. 3.2. SSM/I 24-hour global coverage. Black areas mark regions where the SSM/I does not sense in a 24-hour period (after Hollinger et al., 1987).....	17
Fig. 3.3. SSM/I footprint and swath coverage (after Spencer et al., 1989).....	20
Fig. 3.4. Earth-atmosphere radiative transfer properties (after Liou, 1980).....	25
Fig. 3.5. Vertical atmospheric transmittance for a standard atmosphere (after Liou, 1980)....	27
Fig. 3.6. (a) water and ice Mie volume scattering coefficients for 19.35, 37, and 85.5 GHz, (b) water and ice volume absorption coefficients, (c) water and ice single scattering albedos (after Spencer et al., 1989).....	30
Fig. 3.7. Brightness Temperature response to rain rate for 18, 37, and 85.5 GHz. Results were derived from Wu and Weinman's (1984) radiative transfer model (after Spencer et al., 1989).....	31
Fig. 4.1. Illustrating various terms used in deriving TB anomalies: annulus geometry, right and left boxes, and heading (not to scale).....	39
Fig. 5.1. Scatter diagram of future (24-h)	

	Page
maximum winds (kts) versus 85 GHz vertically polarized average Brightness Temperatures for the the left 55 km box. Correlation coefficient, r , is -0.63	51
Fig. 5.2. As in Fig. 5.1 except only cyclones with a Northwest heading (i.e., in the Northwest quadrant) are considered ($r=-0.81$).....	52
Fig. 5.3. Scatter diagram of future (24-h) maximum winds (kts) versus 85 GHz vertically polarized average Brightness Temperatures for the left 27.5 km box. Only cyclones traveling < 6 kts are considered ($r=-0.83$).....	53
Fig. 5.4. Scatter diagram of future (24-h) maximum winds (kts) versus 19 GHz horizontally polarized average Brightness Temperatures for the left 27.5 km box ($r=0.67$).....	54
Fig. 5.5. Scatter diagram showing relationship between rain and ice signals (19.35H GHz vs 85.5 GHz) for Tropical Storm Greg (after Spencer and Hood, 1989).....	56
Fig. 5.6. Visible imagery of Typhoon Wynne at 2015 UTC on 25 July 1987, which is approximately the same map time used in this study (after Hoffman et al., 1987).....	58
Fig. 5.7. Visible imagery of Typhoon Vernon at 0143 UTC on 20 August 1987 (after Hoffman et al., 1987).....	60
Fig. 5.8. Radar imagery of Typhoon Vernon at 1500 UTC on 20 August 1987 (after Hoffman et al., 1987).....	61
Fig. 5.9. Scatter diagram of future (24-h) maximum winds (kts) versus 85 GHz vertically polarized Brightness Temperature variance for the right 333 km box. Only cyclones traveling < 6 kts are depicted ($r=0.58$).....	62
Fig. 5.10. Scatter diagram of future (24-h)	

	Page
maximum winds (kts) versus 85 GHz vertically polarized TB variance for the left 55 km box. Only cyclones traveling in a northwesterly direction are depicted ($r=0.59$).....	63
Fig. 5.11. Scatter diagram of future (24-h) maximum winds (kts) versus 85 GHz vertically polarized TB anomaly for a right 444 km annulus and the right 222 km interior box ($r=0.55$).....	66
Fig. 5.12. As in Fig. 5.11, except for 19 GHz horizontally polarized TB ($r=-0.51$).....	70
Fig. 5.13. As in Fig. 5.11, except for cyclones traveling < 6 kts only. Note the resulting improvement in correlation, $r=0.69$	72
Fig. 5.14. Scatter diagram of future (24-h) maximum winds (kts) versus 85 GHz vertically polarized TB anomaly for a right 444 km annulus and the right 333 km interior box. Only cyclones traveling < 6 kts are considered ($r=0.82$).....	73
Fig. 5.15. As in Fig. 5.14, except for 19 GHz horizontal polarization and anomaly taken on the left side ($r=-0.77$).....	74
Fig. 5.16. As in Fig. 5.11, except for cyclones traveling in a northwesterly direction ($r=0.61$).....	75
Fig. 5.17. Scatter diagram of future (24-h) maximum winds (kts) versus 85 GHz vertically polarized TB anomaly for a left 444 km annulus and the left 55 km interior box ($r=0.52$).....	77
Fig. 5.18. As in Fig. 5.17, except for cyclones traveling in a northwesterly direction only ($r=0.77$).....	78
Fig. 5.19. As in Fig. 5.18, except for 19 GHz horizontal polarization ($r=-0.75$).....	79
Fig. 5.20. Scatter diagram of future (24-h) maximum winds (kts) versus 85 GHz vertically	

polarized TB anomaly for a left 444 km annulus and the left 27.5 km interior box. Only cyclones traveling < 6 kts are considered ($r=0.81$).....	80
Fig. 5.21. Scatter diagram of future (24-h) maximum winds (kts) versus 85 GHz vertically polarized TB anomaly for a left 333 km annulus and the left 55 km interior box ($r=0.48$).....	81
Fig. 5.22. Scatter diagram of future (24-h) maximum winds (kts) versus 85 GHz vertically polarized TB anomaly for a left 333 km annulus and the left 27.5 km interior box. Only cyclones traveling < 6 kts are considered ($r=0.77$).....	82
Fig. 5.23. Scatter diagram of future (24-h) central pressure change (mb/hr) versus 85 GHz vertically polarized TB anomaly for a right 333 km annulus and the right 222 km interior box. Only deepening cyclones are considered ($r=0.60$).....	85
Fig. 5.24. Scatter diagram of future (24-h) central pressure change (mb/hr) versus 85 GHz vertically polarized TB anomaly for a left 444 km annulus and the left 333 km interior box. Only filling cyclones are considered ($r=-0.65$)..	86
Fig. 5.25. Illustrating relationship between radius (km) and mean delta TB (right-left anomaly).....	93
5.26. Plot of 85 GHz vertically polarized TB anomaly, defined as the difference between the right and left 27.5 km boxes, versus time for eight map times of Typhoon Lynn. Positive numbers indicate lower mean TB values in the left box. Future (24-h) central pressure change (CPC), in mb/hr, is also shown. Positive numbers depict deepening.....	96
Fig. 5.27. As in Fig. 5.26, except for the 55 km case.....	97

	Page
Fig. 5.28. As in Fig. 5.26, except for the 111 km case.....	98
Fig. 5.29. As in Fig. 5.26, except for the 222 km case.....	99
Fig. 5.30. As in Fig. 5.26, except for the 444 km case.....	100
Fig. 5.31. Progression of minimum TB's during Lynn's lifecycle. The box radius containing that TB is indicated.....	104
Fig. 5.32. Behavior of Lynn's TB anomalies (defined as difference between right and left box mean 85 GHz vertically polarized TB's) for all box radii. Lines shown are the map times for which future (24-h) maximum sustained winds are < 50 kts. Positive delta TB values indicate lower TB's on the left side of the cyclone.....	105
Fig. 5.33. As in Fig. 5.32, except for map times containing winds > 50 kts.....	106
Fig. 5.34. Plot of 85 GHz vertically polarized TB anomaly (defined as the difference between mean TB in the right 444 km annulus and mean TB in the right 111 km box), versus time for eight map times of Typhoon Lynn. Future (24-h) central pressure change (CPC), in mb/hr, is also shown (positive numbers depict deepening).....	108
Fig. 5.35. As in Fig. 5.34, but for TB anomaly defined on the left side.....	109
Fig. 5.36. As in Fig. 5.34, but for anomaly defined as the difference between mean TB in the right 444 km annulus and mean TB in the right 55 km box.....	110
Fig. 5.37. As in Fig. 5.36, except for the left side of the cyclone.....	111
Fig. 5.38. Cross section of average 85 GHz vertically polarized Brightness Temperatures	

	Page
for Typhoon Lynn on 17 October 1937 at 2000 UTC (early phase).....	113
Fig. 5.39. As in Fig. 5.38, but relates to 18 October 1987 at 0830 UTC.....	114
Fig. 5.40. As in Fig. 5.38, but relates to 21 October 1987 at 2100 UTC, near time of maximum intensity.....	115
5.41. As in Fig. 5.38, but relates to 25 October 1987 at 1030 UTC.....	116
Fig. 5.42. As in Fig. 5.38, but relates to 26 October 1987 at 1000 UTC, just prior to dissipation.....	117
Fig. 5.43. As in Fig. 5.39, except for 19 GHz horizontal polarization.....	119
Fig. 5.44. As in Fig. 5.43, but relates to 24 October 1987 at 2200 UTC.....	120
Fig. 5.45. As in Fig. 5.41, except for 19 GHz horizontal polarization.....	121
Fig. 5.46. As in Fig. 5.45, but relates to 25 October 1987 at 2200 UTC.....	122

DIGEST

Microwave data from the Special Sensor Microwave Imager (SSM/I) were obtained for twenty-nine map times of tropical cyclones from the Northwest Pacific and North Indian Ocean. Automated analysis of 85 GHz vertical polarization (85V GHz) Brightness Temperatures (TB's) were conducted by calculating statistics at various radii from a cyclone center. These statistics were correlated against storm traits such as intensity, vortex translation speed, central pressure changes, and direction of vortex movement.

The aim of this research was to determine relationships between 85V GHz data and cyclone characteristics, which could lead to the development of forecasting tools using SSM/I data. Anomalies in the 85V GHz TB fields demonstrated strong correlations to cyclone intensification by highlighting the positions and orientations of the principal rain bands. Such anomalies reveal asymmetries of convection associated with spiraling rainbands and convective eyewalls.

This research demonstrated that SSM/I derived TB fields can show patterns of high correlations in the anomalies, as well as portray processes associated with intensification that occur in a tropical cyclone. Since these results were achieved through automatic methods, it is possible to develop forecast nomograms that link SSM/I TB data to cyclone traits. Such tools would be useful in the prediction of tropical cyclones.



Accession For	
NTIS GRA&I	<input checked="" type="checkbox"/>
DTIC TAB	<input type="checkbox"/>
Unannounced	<input type="checkbox"/>
Justification	
By	
Distribution/	
Availability Codes	
Dist	Avail and/or Special
A-1	

CHAPTER I. INTRODUCTION

Each year hurricanes and typhoons cause vast amounts of damage and a large number of deaths and injuries. The damage can be especially devastating in the tropics where many small countries and islands are often in the direct path of horrifying cyclones. Super Typhoon Nina, for example, killed approximately 658 people in southern Luzon (in the Philippine Islands) just after devastating the island of Truk (Hoffman et al., 1987). The need for accurate forecasting of these storms is clearly of extreme importance.

Prior to October 1987, the U.S. Air Force routinely flew aerial reconnaissance missions to collect weather data on western Pacific tropical cyclones. Such data included latitude-longitude fixes of the eye, measurements of winds, temperature and pressure, and any other information needed by operational weather forecasters to accurately predict an impending storm's movement and intensification. This program, however, ended in 1987 due to budgetary reasons, creating a void of

tropical cyclone information in the Pacific. Attention then turned to the Special Sensor Microwave Imager (SSM/I), a new instrument aboard a Defense Meteorological Satellite Program (DMSP) spacecraft, as a hopeful replacement of the valuable cyclone data once provided by aerial reconnaissance.

Launched in June 1987, the SSM/I provides a new type of data base from which researchers and operational forecasters can draw. The data is in the form of Brightness Temperatures (TB's) which are derived from four different frequencies of microwave emissions from the earth's surface and atmosphere. The SSM/I offers global coverage of storms and provides the opportunity to improve the prediction of tropical cyclones. Much remains to be learned from this relatively recent data, including its relationship to tropical cyclone traits.

This research attempts to analyze, in a uniform and automated fashion, the SSM/I-measured TB fields of tropical cyclones. Such analysis will determine to what extent relationships between TB patterns and certain cyclone characteristics exist.

Specifically:

1) Statistics of the TB fields from 29 tropical cyclones will be stratified according to cyclone trait. Characteristics of most importance to the meteorological community would be future intensity changes (i.e., changes in the maximum sustained wind speed or central pressure), vortex translation speed, and directional changes.

2) The TB fields and their anomalies will be scrutinized to see if high correlations to these traits are achieved. It is hypothesized the TB fields will reveal asymmetries within a cyclone that would mark areas of temperature gradients and differences in hydrometeors. These would affect the maturation of the typhoon.

3) A case study of one typhoon will also be conducted in order to observe any unique patterns emerging within the cyclone's lifecycle; a kind of "internal stratification."

If such relationships between cyclone traits

and patterns of TB's exist, rules can be developed that would greatly aid the operational forecaster having access to SSM/I data.

CHAPTER II. Review of Related Literature

Atmospheric remote sensing of microwave emissions is a relatively recent endeavor. The majority of remote sensing studies began in the late seventies to early eighties using microwave radiometers aboard aircraft. Specific applications of microwave signatures to physical processes within tropical cyclones are currently being made. The SSM/I data afforded a new opportunity to broaden the existing knowledge of tropical cyclones and many other meteorological systems. It opened up a new arena for the exploration of forecasting aides using microwave Brightness Temperatures (TB's). Previous research (e.g., Rhudy, 1989) has provided clues that strong relationships exist between a cyclone's TB field and its traits (e.g., intensity). Indeed, many researchers have found microwave data to reveal some characteristics of tropical cyclones not otherwise shown by conventional data.

Among the first scientists to relate satellite Visible (VIS) and Infrared (IR) imagery to tropical cyclone intensity change was Dvorak (1975, 1984),

who introduced a technique for determining cyclone wind speeds from satellite data. The Dvorak technique is widely used to determine cyclone intensity, and in the present study such intensity is correlated with the anomaly of the TB field. Gentry et al. (1980) determined that IR measurements of Equivalent Blackbody Temperatures (TBB) of cloud tops over the inner core are well correlated to a storm's future intensity (24-hour maximum winds). Later, Steranka et al. (1986) supported these findings by showing the average cloud top temperature within a 222 km radius of the center to be an excellent indicator of a cyclone's strength, its distribution of convective elements, and latent heat storage. Moreover, they found a lag time of 24 hours between the onset of convection and the increase of maximum winds, which supports the theoretical relationship between latent heat release and generation of kinetic energy. These findings suggest that the TBB field could be used to forecast a storm's intensity changes.

Similar and perhaps superior capabilities exist with the microwave data. For example, Rodgers and

Adler's (1981) microwave data, sensed by the ESMR-5 satellite, showed cyclone intensification signals not seen in associated IR or VIS imagery. Such signals included an increasing rain rate as the TB increased. Other signals highlighted inward-moving spiral rainbands with increasing intensity, and the earlier detection of eye formation. Such detection is not usually feasible through VIS or IR means, and consequently not reported. However, through examination of the increasing curvatures of the inward-moving rainbands (which are accompanied by a decrease in the radius of the maximum rain rate), the location of the eye can be discerned through microwave data.

Both Wilheit et al. (1982) and Adler et al. (1990) used microwave radiometers aboard aircraft to observe tropical storm rain cells, illustrating the relationships between the measured TB and rain rates within a storm. They found that very low TB in the higher frequencies (near 85 GHz) were associated with ice scattering above the rain areas, while the lower frequencies (near 19 GHz) responded more readily to lower level liquid precipitation and

surface influences. Fig. 2.1, from the study of Adler et al., shows the behavior of several frequencies along two aircraft tracks. Note the dramatic response in the microwave frequencies to storm parameters as compared to the 11 micrometer IR plot.

The most recent research used SSM/I data to support the idea that microwave imagery is a viable candidate for serving as a typhoon intensity predictor. Holliday and Waters (1989), for example, showed how SSM/I data could be used to detect gale force winds in rain-free areas. These areas can extend well beyond the rain areas, and are an intensity indicator. Furthermore, Rao et al. (1989) determined that SSM/I data compared well with observed winds, and supported Rodgers and Adler's latent heat estimates. They found that rain drops impacting the ocean surface, however, can cause SSM/I derived winds to be overestimated. As wind speed increases, though, the influence of rain impaction becomes secondary to the affect of wind-induced sea roughness, illustrating the benefit of the higher level SSM/I 85 GHz channel. Lee and

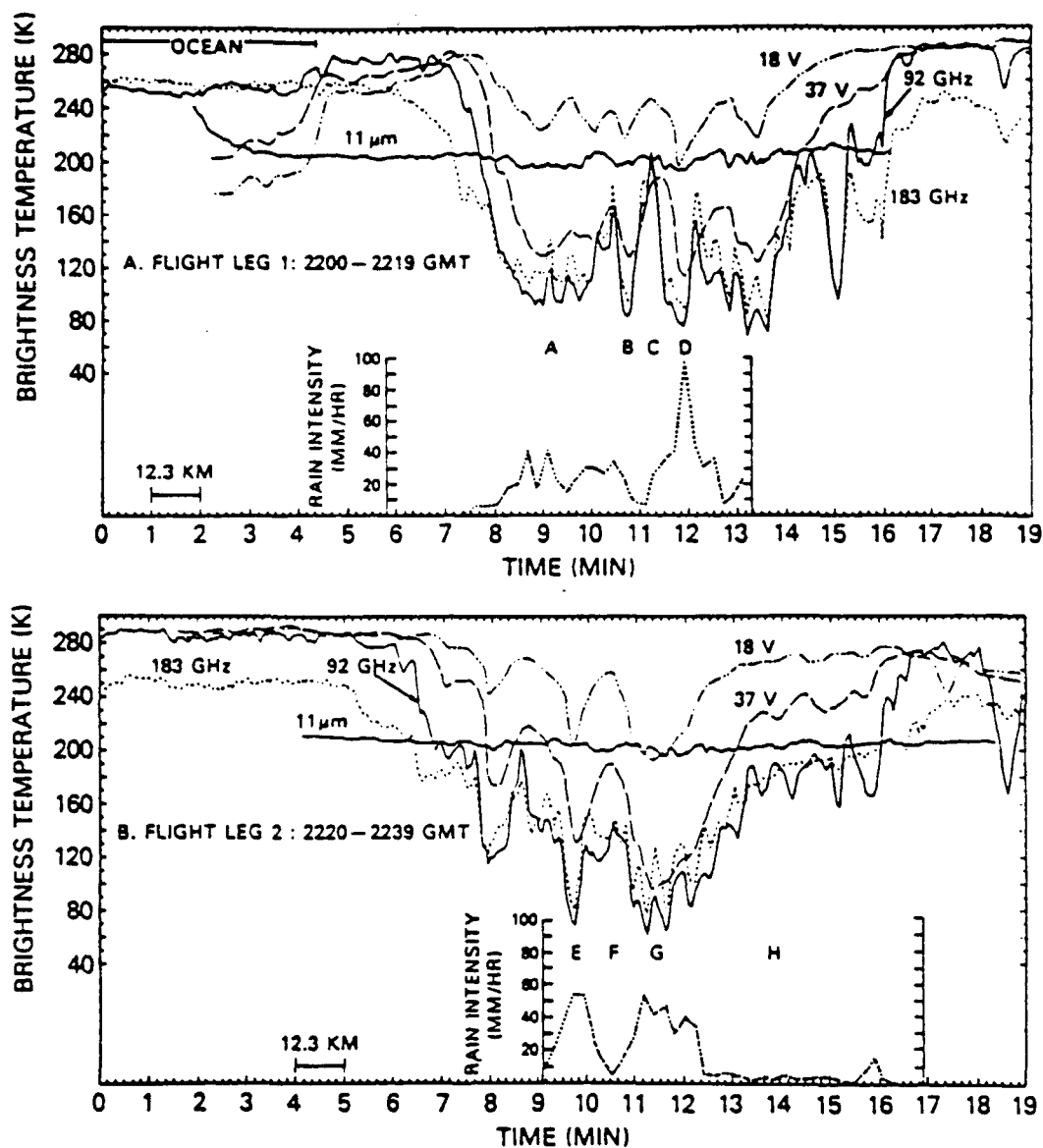


Fig. 2.1. Two aircraft flight legs of TB measurements over a thunderstorm complex. Various microwave frequencies and one IR frequency, 11 micrometers, are shown (after Adler et al., 1990).

Caughey (1989) called attention to the ability of the 85 GHz frequency in improving the Dvorak technique by depicting the formation of an eye where other data sources lacked such capability. Lee and Caughey also concluded that 85 GHz was preferred in portraying convective areas as well as the asymmetries of convection in the eyewall region of a tropical cyclone.

Such asymmetries have been shown to be important in developing cyclones. For example, Burpee and Black (1989) found higher rain rates in conjunction with asymmetric eyewalls than with concentric eyewalls, which occur in the later stages of a cyclone. Merrill (1988) found open streamlines to occur in hurricanes that were intensifying, while non-intensifying cyclones had constricted, or closed streamlines. Other studies showed that anomalies in the 85 GHz TB pattern had good correlations to future (24-hour) intensity (Rhudy, 1989). Fiorino and Elsberry (1989) illustrated the presence of cyclonic gyres to the west of cyclone centers, and anticyclonic gyres to the east. TB anomalies may reveal this effect as well.

Many studies showed SSM/I data to be capable of depicting not only intensification processes, but a variety of storm characteristics as well. Spencer and Hood (1989) found high correlations between microwave imagery at 85 GHz (corrected for polarization) and rain gauge data from a long-lived squall line, thus supporting the studies of Wilheit et al. (1982). The work of Glass and Felde (1989), as well as Lee and Caughey (1989), illustrated how the SSM/I data, especially the 85 GHz channel, provided important storm information where the IR and VIS data fell short. Such information included a distinct delineation of rain areas from non-rain areas. Ferraro et al. (1989) also suggest that 85 GHz gives the most information relative to precipitation areas.

Vortex translation speed and direction of motion have also been depicted in microwave studies. The studies of Burpee and Black (1989) indicated that translation speed was one of several factors that would influence asymmetrical rain patterns within the eyewall region. Moreover, Shapiro (1983)

found that storms moving at 10 m/s had their maximum rain rates to the right of the storm track. TB asymmetries in the inner regions of a cyclone, therefore, may reflect such patterns when compared to intensity and translation speed.

Additionally, Fiorino and Elsberry (1989), have suggested that the outer regions of a tropical cyclone (beyond 300 km radius) are more related to speed of movement than are the inner regions. This is related to the idea of an effective radius which describes an inner envelope through which a cyclone maintains its identity from the outer environment. The movement of the cyclone is dependent upon its interaction with the environment at some unique radius from the eye (Holland, 1983). Carr and Elsberry (1990), however, point out that many other processes may be involved in cyclone propagation. Such processes included sea surface temperature, dynamic processes occurring in the core itself, and "self advection" of the cyclone, induced by asymmetrical flow as described by the cyclonic and anticyclonic gyres (Fiorino and Elsberry, 1989).

Willoughby et al. 1984 and Willoughby, 1988 describe many of the processes that take place within and around the tropical cyclone core. As indicated above, motion and even intensification, resulting from asymmetries within the cyclone core are still poorly understood. Willoughby showed how asymmetrical rainbands, which may be Rossby or internal gravity waves, act as asymptotes that separate outer environmental air from inner cyclone flow. These bands, which are 5 to 50 km thick, cover the inner 100 to 300 km radius and spiral inward toward the center.

Some cyclones have stationary bands, while others rotating. Stationary bands have been shown to be related to deviations in movement of the center, and are a result of asymmetric forcings. Shapiro (1983) described the asymmetric configuration of these bands as being related to vortex translation and environmental flow interactions, which result in boundary layer convergence in areas beneath the rainbands.

Willoughby's (1988) research also supports some

of the findings of Rodgers and Adler (1981) mentioned earlier. Specifically, as a cyclone intensifies, the bands move inward and encircle the eye. The resulting outer eyewalls then replace existing inner eyewalls at the maximum intensity stage of the cyclone. Since the rainbands contain convective elements that move through the large stratiform rain area (Powell, 1990), SSM/I TB should depict the orientation of the bands and their changing patterns with intensity.

From the research discussed above, it is apparent the SSM/I data can be a valuable forecasting tool by depicting certain physical processes within a cyclone. This research further developed the ideas expressed earlier by Rhudy (1989), by expanding the data base, examining TB signatures in greater depth, and automating the entire analysis operation. Many of the processes and phenomena discussed above were evident in the patterns of the SSM/I TB field found in the present research, as were other features of cyclone intensification.

CHAPTER III. THE MICROWAVE IMAGER AND DATA

a. *The Special Sensor Microwave Imager*

The SSM/I, housed aboard the DMSP spacecraft F8, passively measures microwave emissions from the surface and atmosphere as it traverses the earth in an ascending sun synchronous polar orbit. The phrase "ascending sun-synchronous" refers to the satellite crossing the equator (traveling from south to north) at the same local time each day. In this case that time is 0612L. As shown in Fig. 3.1, the satellite travels at 6.58 km/sec at an altitude of 833 km above the earth. This gives an orbital period of 102 minutes, resulting in 14.1 revolutions of the satellite around the earth each day. Fig. 3.2 shows the coverage of the SSM/I over a 24-h period. Such global coverage offers a great opportunity to study weather phenomena in a manner not previously available.

The SSM/I instrument faces aft (with respect to the satellite's direction of travel), and senses downward at an angle of 45 degrees (Fig. 3.1). As

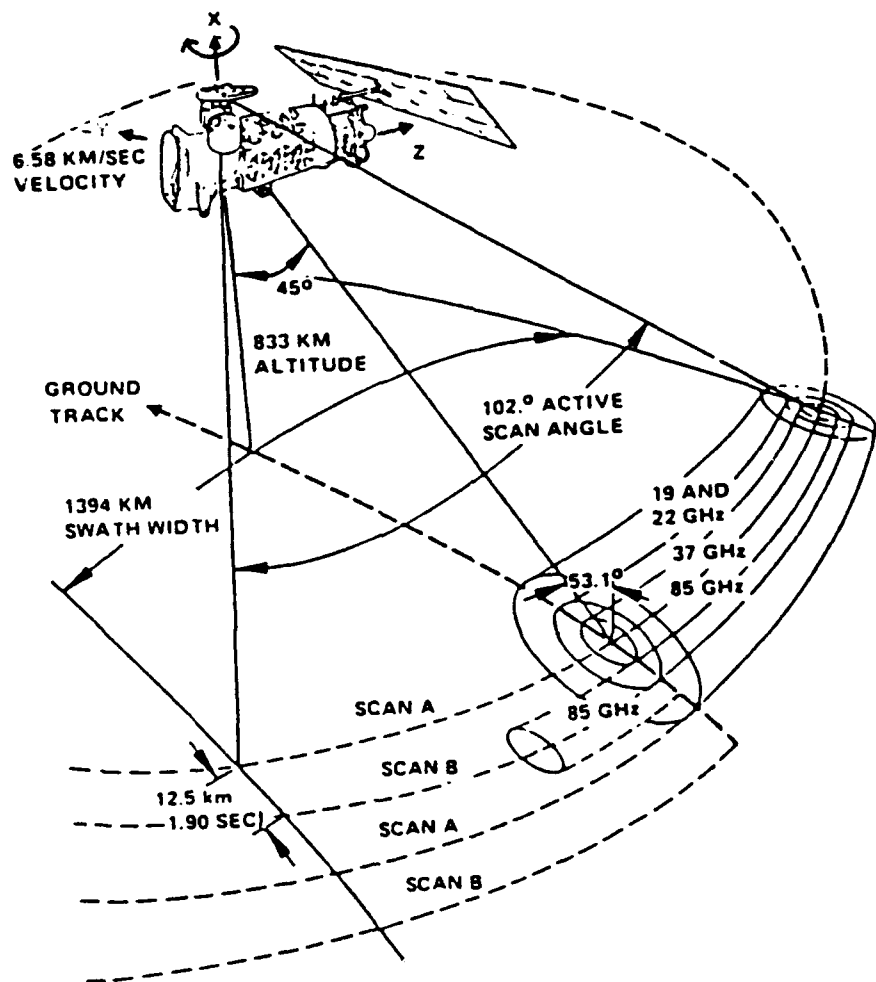


Fig. 3.1. SSM/I scan geometry. The satellite travels in the direction marked "subtrack" while the SSM/I instrument rotates around the axis labeled "x" (after Hollinger et al., 1987).

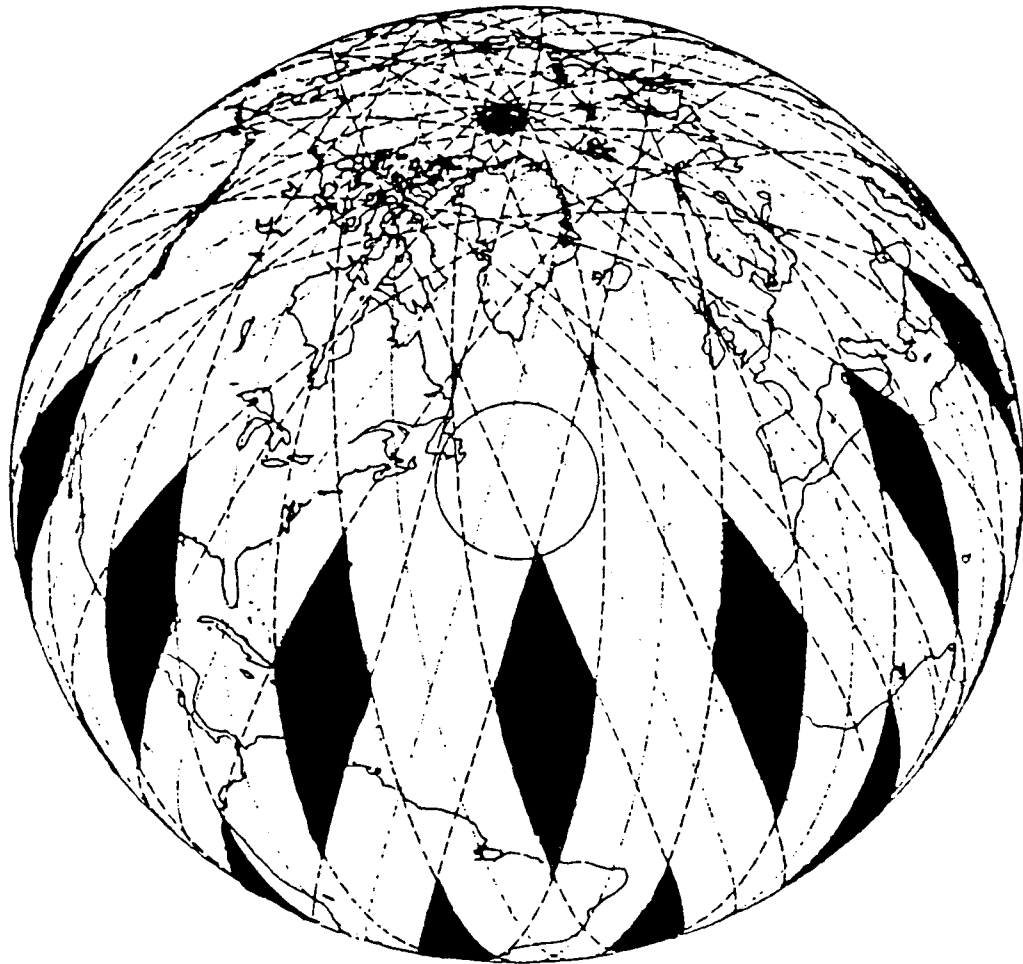


Fig. 3.2. SSM/I 24-hour global coverage. Black areas mark regions where the SSM/I does not sense in a 24-hour period (after Hollinger et al., 1987).

the satellite orbits the earth, the SSM/I rotates at 31.6 rpm (from left to right when looking aft), parallel to the local vertical of the satellite. This produces a scan swath of 1394 km (or a 102.4 degree scan angle) about the satellite subtrack (the subtrack is defined as the path along the earth's surface directly below the satellite). Between each SSM/I rotation, the satellite travels a subtrack distance of 12.5 km. This results in a 12.5 km separation between each scan, which is referred to as the resolution.

During each scan, the SSM/I measures radiation emitted by the earth-atmosphere system at four microwave frequencies: 19.35, 22.235, 37.0, and 85.5 GHz. Except for 22 GHz, the SSM/I measures two polarizations (vertical and horizontal) for each frequency. At 22 GHz only vertical polarization is used, which results in seven channels sensed by the SSM/I. Due to the look-down angle of the instrument, vertical polarization refers to the 45 degree plane, while the horizontal polarization is perpendicular to that. With vertical polarization, the SSM/I senses more emitted radiation from the

atmosphere, while more surface features are sensed through the horizontal.

Along the 1394 km swath, a scan at 85 GHz collects radiation from 128 pixel points (at 12.5 km resolution). For the remaining channels, however, the instrument only collects data on every other scan, resulting in 64 pixels of data. This provides a 25 km resolution for all frequencies except 85 GHz. Fig. 3.1 depicts these two types of scans as A (all channels) and B (85 GHz only). Each frequency also has a different sized footprint, as shown in Fig. 3.3. Note that 85 GHz has the best resolution and the smallest footprint (15x13 km), while 19 GHz has the largest (69x43 km). The imager actually senses an average emission within a given footprint. Hollinger et al. (1987) offer a more detailed explanation of these SSM/I parameters.

b. *The data*

When a sensor collects data, it is measuring radiation emitted from the earth-atmosphere system and space. Such emission is converted into

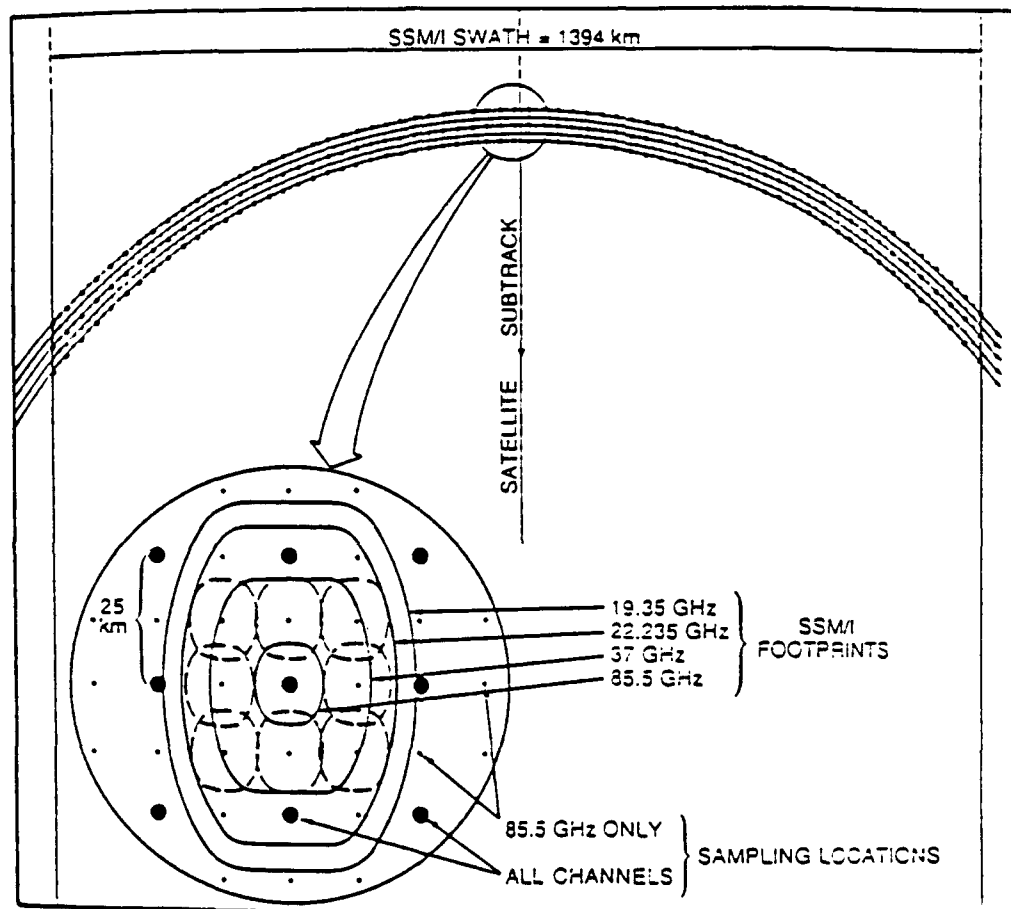


Fig. 3.3. SSM/I footprint and swath coverage (after Spencer et al., 1989).

Brightness Temperature by applying Planck's law. In radiative transfer theory, the term "blackbody" is used to describe a theoretical body that emits (and absorbs) radiation perfectly and equally in all directions. The intensity of that radiation (B) is related to the physical temperature (T) of the object by the Planck function (in the frequency domain):

$$B_\nu(T) = 2h\nu^3/[c^2(e^{h\nu/KT} - 1)] \quad (1)$$

where h is Plank's constant, K is Boltzmann's constant, c is the velocity of light, and ν is the frequency.

In the microwave regime, however, $h\nu/KT \ll 1$. Therefore, (1) can be approximated as follows:

$$B_\nu(T) \approx (2K\nu^2/c^2)T \quad (2)$$

This describes a linear relationship of radiance to temperature, which is referred to as the Rayleigh-Jeans law (Liou, 1980). However, this is for a perfect blackbody, which does not exist. In

applying this theory to actual measurements of the earth, the following expression is used:

$$I_{\nu} = (2K\nu^3/c^2)TB(\nu) \quad (3)$$

where I_{ν} denotes non-blackbody radiance at frequency ν and $TB(\nu)$ refers to the Equivalent Brightness Temperature at the same frequency. Since a blackbody emits perfectly and a non-blackbody does not, the difference between T and TB above is therefore a matter of emissivity, ϵ . From (2) and (3),

$$\epsilon = \frac{I_{\nu}}{B_{\nu}} \quad \text{or} \quad \frac{TB}{T} \quad (4)$$

therefore,

$$TB = \epsilon T \quad (5)$$

Emissivity varies greatly depending upon the surface type, polarization, and frequency used. Since ϵ is always between 0 and 1 ($\epsilon = 1$ for a blackbody), (5) shows that the Brightness

Temperature will always be less than the physical temperature of the emitter.

The arrival at TB values from the actual measurements at the SSM/I antenna reflector is accomplished by calibrating the raw input against near-blackbody and cold space references. This is done for each scan, through which an antenna temperature (TA) is achieved. The TA reflects the temperature sensed at the antenna, but contains spurious affects from the antenna side lobes and other undesirable influences. An antenna pattern correction is then applied which results in the Equivalent Brightness Temperature. The TB's are stored in the form of Sensor Data Records (SDR) which are the values used in this research. From the SDR's available at each pixel point the Environmental Data Records (EDR's) are derived. Such environmental parameters include wind speed, rainfall, cloud water, etc. Hollinger et al. (1987) provide a detailed discussion of the above processes.

c. Microwave radiative transfer properties

Microwave emissions sensed by the SSM/I are affected by atmospheric and surface attributes. These emissions can originate from a combination of atmosphere, surface, or reflected radiation as illustrated in Fig. 3.4. Moreover, these attributes affect each frequency differently through attenuation processes such as absorption and scattering. In order to correctly interpret SSM/I TB data, it is therefore necessary to understand how these emissions are influenced between the emitting source and the sensor.

The principle atmospheric properties affecting microwave radiation are water vapor, liquid precipitation, ice and oxygen. The magnitude of the influence depends on such parameters as drop size distribution, cloud thickness, rain rate, and the presence of ice particles. Precipitation and water vapor do not affect the longer wavelengths of microwave radiation in the same manner as they do the infrared (IR) spectrum. In fact, clouds and rain increase microwave emission while obscuring IR emission. This leads to one of the advantages of

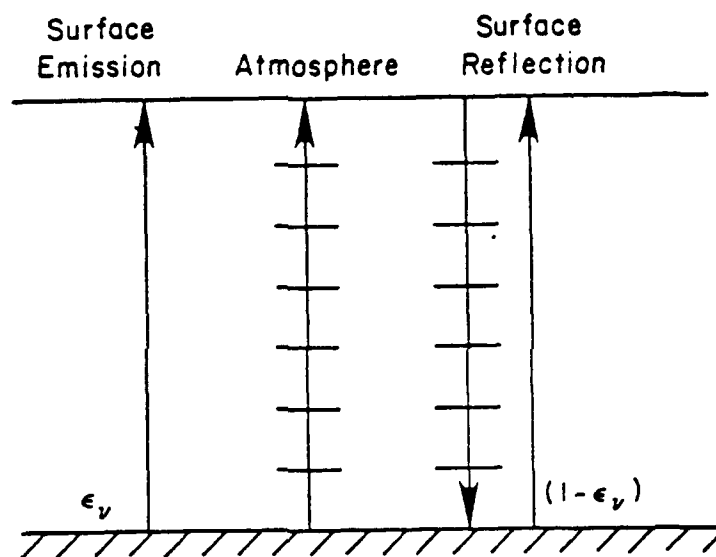


Fig. 3.4. Earth-atmosphere radiative transfer properties (after Liou, 1980).

microwave over IR; much of the latter is absorbed by water vapor, providing imagery of only cloud tops. Much of the microwave emissions, on the other hand, radiate through and from cloud water vapor (depending on the frequency), allowing views of atmospheric features not otherwise seen.

As microwave frequency increases, cloud water, ice and liquid precipitation influences generally increase. This means the longer wavelengths or the lower frequencies are able to penetrate more atmosphere before attenuation occurs. In effect, the SSM/I radiometer can observe deeper into the atmosphere at lower frequencies, while higher frequencies portray higher elevations. The latter occurs due to absorption and reemission at cloud height, resulting in lower TB values. Fig. 3.5 illustrates this by a general decline in transmittance with increasing frequency (except for water vapor absorption bands at 22.235 GHz and 183 GHz, and oxygen absorption bands near 60 and 120 GHz). However, this is greatly complicated by the effects of the constituents of the target area being sensed and the underlying surface properties.

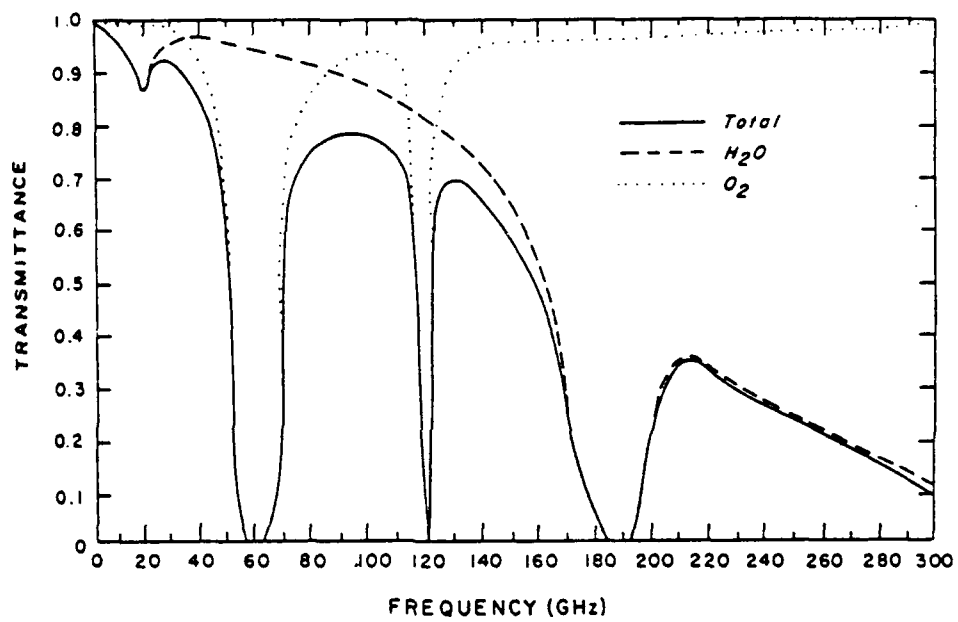


Fig. 3.5. Vertical atmospheric transmittance for a standard atmosphere (after Liou, 1980).

Moreover, each frequency reacts differently to these influences.

Understanding the surface components is very important when interpreting TB data. Due to the low emissivity of water and to its highly reflective nature, the ocean is radiometrically cold. Land, on the other hand, generally has higher emissivities (depending upon soil content and vegetation), which result in warmer TB's. The TB values measured at the different SSM/I channels, therefore, vary depending upon ocean versus land backgrounds. This research concentrates on over-ocean tropical cyclones, discarding any cyclone whose TB measurements are contaminated by land emissivities.

The presence of water vapor and cloud droplets over an ocean surface causes increased microwave emissions and therefore warm TB's. The presence of rain causes TB's to increase even further, as the water absorbs and re-emits radiation from below. The lower frequencies, however, respond more readily to liquid precipitation than they do to the presence of cloud droplets. Higher frequencies, on the other

hand, respond more quickly to scattering processes through the presence of large non-spherical rain drops and ice. Fig. 3.6, for example, depicts the greater sensitivity of 85 GHz to the presence of ice as compared to 19 GHz (Spencer et al., 1989).

Therefore, as the rain rate within a target area increases, all frequencies respond with increasing TB values, but more so at lower frequencies. Wilheit (1977), however, showed that as the rain rate increased there was an increase in the frequency of larger rain drops. Beyond a critical rain rate, therefore, the intrusion of larger rain drops and ice scatter away the upwelling radiation. This results in a drop in TB value, especially at higher frequencies as explained above. Such behavior is illustrated in Fig. 3.7. Within a tropical cyclone eye region, however, warmer TB's would be expected at higher frequencies due to high water vapor and fewer scattering hydrometeors.

As shown by Spencer and Hood (1989), there is an inverse relationship between 19 and 85 GHz. In the presence of heavy rain, as the 19 GHz values

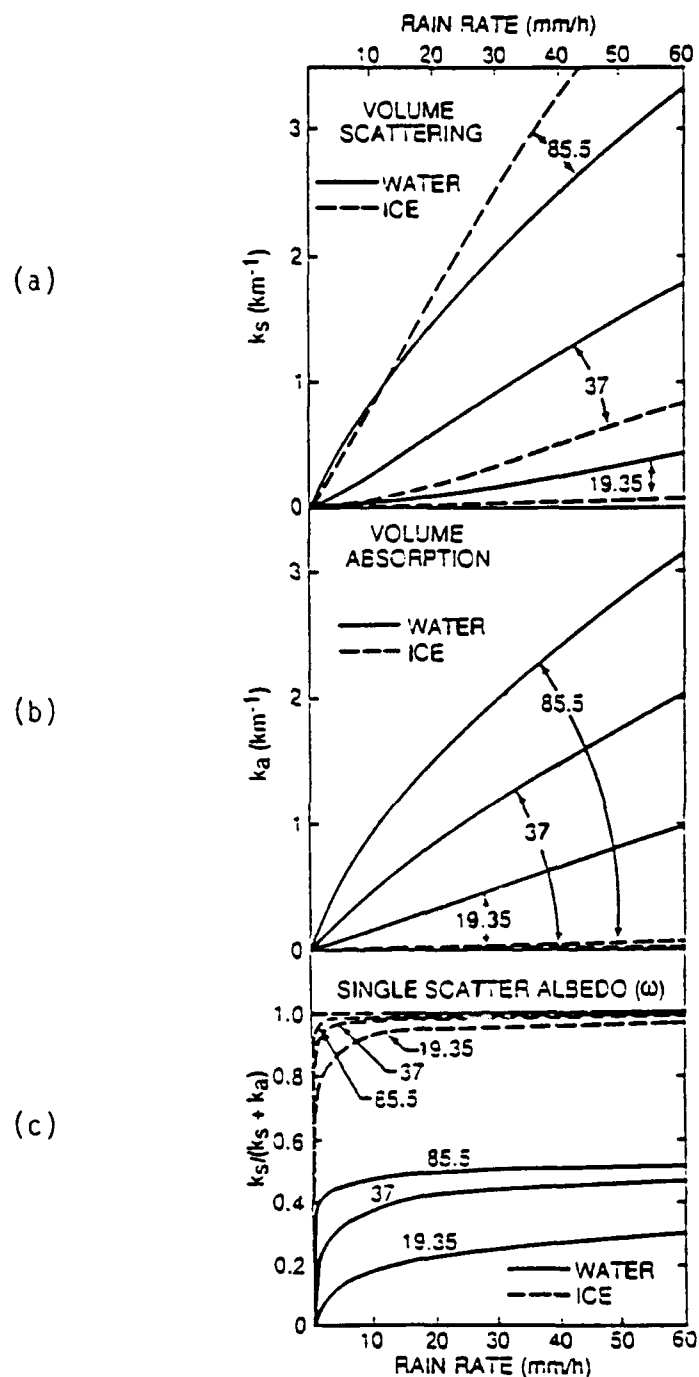


Fig. 3.6. (a) water and ice Mie volume scattering coefficients for 19.35, 37, and 85.5 GHz, (b) water and ice volume absorption coefficients, (c) water and ice single scattering albedos (after Spencer et al., 1989).

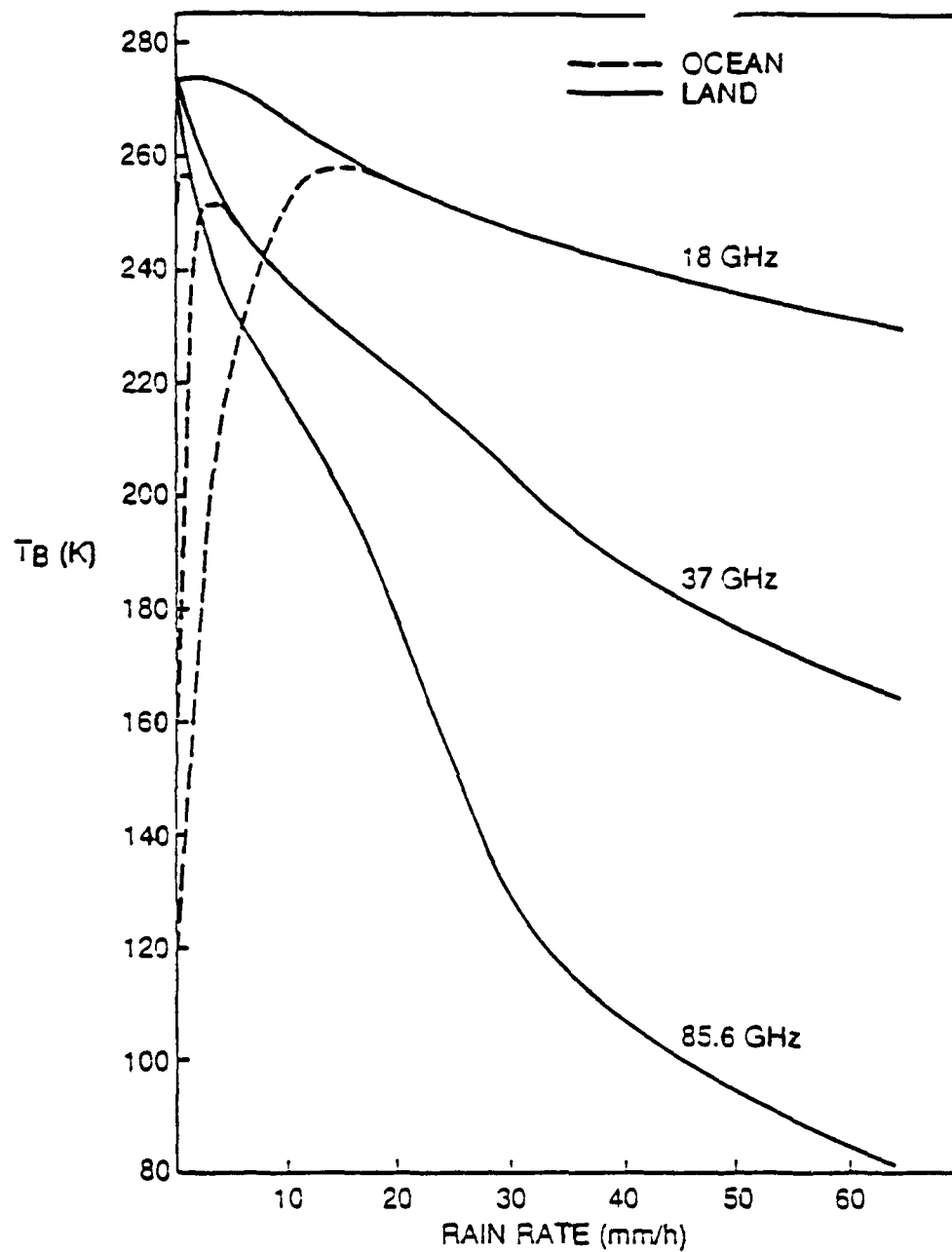


Fig. 3.7. Brightness Temperature response to rain rate for 18, 37, and 85.5 GHz. Results were derived from Wu and Weinman's (1984) radiative transfer model (after Spencer et al., 1989).

rise, the 85 GHz TB's decrease. This is caused by two factors: 1) the higher frequencies (85 GHz) respond much more readily to scattering hydrometers than do the lower channels. 2) The lower frequencies, especially 19 GHz, react to the emissivity of the surface. In the latter case, the churned up seas within a tropical cyclone would greatly enhance emission, and thereby raise TB values. Rain impaction would also cause greater emissions at 19 GHz, but as Rao et al. (1989) indicate, roughness caused by high winds is of primary importance. These effects were illustrated in the present research as well, and will be shown in Chapter V.

The dual polarization capability in the SSM/I is also important in analyzing the TB data at different frequencies. For example, cold TB measurements at 85 GHz can result from a dry atmosphere, as well as from a highly convective rain area containing scattering hydrometeors. Since TB resulting from ocean reflection is polarized and TB values resulting from scattering effects are not, the vertical and horizontal polarizations can be

used to determine oceanic influence (Wilheit et al., 1982 and Spencer and Hood, 1989). In the present research, vertical polarization was chosen for 85 GHz, while horizontal was chosen for 19 GHz. The former provides more information about the atmosphere, and the latter reveals the surface properties.

It is therefore evident that higher microwave frequencies would depict, by TB depression, the convective regions of tropical cyclones and respond inversely to increasing rain rates (due to the expected presence of large rain drops and possibly ice). Indeed, this has been shown in earlier studies, and was examined in this research with 85 GHz. The behavior of the SSM/I-measured 85 GHz emissions, as discussed above, reveals certain properties of tropical cyclones. This is especially true when these results are compared to lower frequencies (19 GHz in this study), and when both vertical and horizontal polarizations are applied.

CHAPTER IV. THE PROCEDURE/METHODOLOGY

a. *Data collection*

The SSM/I data used in this study were obtained from the archives of the Naval Research Laboratory in Washington, D.C., through the Air Force Geophysics Laboratory (AFGL), at Hanscom Air Force Base, MA. The data, in the form of Sensor Data Records (SDR's), were loaded on magnetic tape and shipped to St. Louis University for SSM/I research. The SDR's were organized by polar orbit flown by the satellite F8. For example, orbit number 1692 provided the first map time over typhoon Lynn, while number 1698 was the next orbit passing over that cyclone.

The desired orbits, however, had to be determined in order to request the correct data. Using the Annual Tropical Cyclone Report (Hoffman, et al., 1987 and Plante and McMorro, 1988), all tropical cyclones (reaching at least tropical storm status) from the Northwest Pacific and North Indian Oceans during 1987 and 1988 were plotted on a polar

stereographic chart. This time period was chosen because of the abundance of available data, and over-ocean tropical storms were desired for study.

Next, with the aide of SSM/I ascending nodal crossing data (Conway, 1989), an orbit wheel was constructed on the chart to enable identification of which satellite orbits, and at what precise point of the orbit, passage over a storm occurred. The segment of the orbit covering the cyclone was then calculated as seconds into the day (UTC). This calculated time period would be used to download the precise data segment from magnetic tape, and would contain the TB distribution of the storm. Although as many cyclone map times as possible were pursued, only orbits having adequate sensor coverage (defined as the satellite subtrack passing within three degrees of the cyclone path) were used. Cyclones contaminated by land were also discarded. The resulting 29 cyclone map times used in this study, are shown in Table 4.1.

Once the appropriate SDR's were received from AFGL, the St. Louis University VAX/VMS computer was

<u>NAME</u>	<u>ORBIT</u>	<u>DATE</u>	<u>TIME (UTC)</u>
Vernon	428	07/20/87	1000
Wynne	505	07/25/87	2030
Alex	506	07/25/87	2200
Alex	513	07/26/87	1030
Cary	788	08/14/87	2115

Dinah	929	08/24/87	2100
Dinah	936	08/25/87	0930
Dinah	1000	08/29/87	2141
Dinah	1007	08/30/87	1009
Holly	1104	09/06/87	0700

Freda	1106	09/06/87	0900
Holly	1147	09/09/87	0800
Holly	1161	09/10/87	0800
Freda	1176	09/11/87	0930
Ian	1416	09/28/87	0930

Kelly	1621	10/12/87	2100
Kelly	1635	10/13/87	2050
Kelly	1643	10/14/87	0930
04B	1651	10/15/87	0000

Lynn	1692	10/17/87	2000
Lynn	1698	10/18/87	0830
Lynn	1712	10/19/87	0820
Lynn	1748	10/21/87	2100
Lynn	1791	10/24/87	2200

Lynn	1798	10/25/87	1030
Lynn	1805	10/25/87	2200
Lynn	1812	10/26/87	1000
Nina	2200	11/22/87	2100
Susan	4912	06/01/88	2230

Table 4.1. SSM/I map times of typhoons and one tropical cyclone (04B) used in this study.

accessed to download the data from tape to disk. Software provided by AFGL was used to accomplish this, and required the time segments for each orbit number as input. This allowed extraction from the SDR files, the desired portion of the orbits containing SSM/I measurements over selected cyclones. These segments were then stored on the VAX computer disk by orbit number.

b. Calculation of statistics

Once residing on disk, statistical analysis could be applied to the TB distribution of each cyclone map time. AFGL software, residing on the St. Louis VAX computer, was once again accessed for this task.

The first step involved converting the TB distributions, as measured by the SSM/I, from Polar to Mercator projection. Mercator projection would allow for more ease in the analysis of the TB values. The computer program loaded the data from a given orbit file (containing the precise segment of data collected while the satellite was over the

cyclone) into a second disk file. This file was organized as a matrix of grid points spaced 10 km apart, over which each SSM/I scan was laid. Where the data points within the scan did not match the grid points, a replication was employed to assign an appropriate value to the Mercator grid point. Where a matrix grid point fell outside of the SSM/I scan, a value of zero was assigned.

The next step involved the use of another program that calculated the mean, maximum, minimum, standard deviation and variance, of the TB distribution for each map time. To do this, various boxes were drawn centered on the eye of each storm, and oriented to the direction of movement (see Fig. 4.1). The latitudes and longitudes of the cyclone centers were derived from Hoffman (1987) and Plante and McMorrow (1988), while cyclone heading information was taken from the Hong Kong Royal Observatory (1987, 1988) manuals. The boxes varied in size from 55 km X 55 km, to 888 km X 888 km. The above statistics were then calculated for each half of a box, making the variation in box size 27.5 km X 55 km, to 444 km X 888 km, for both sides of the

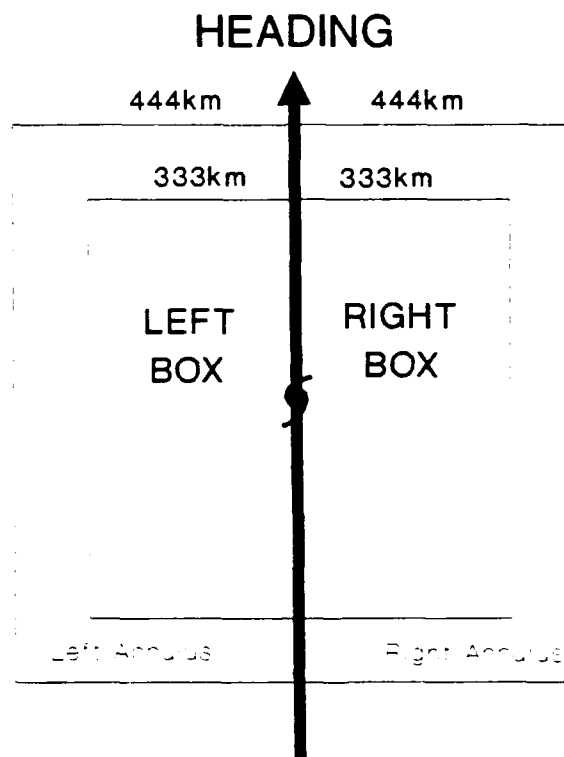


Fig. 4.1. Illustrating various terms used in deriving TB anomalies: annulus geometry, right and left boxes, and heading (not to scale).

cyclone. Thus, as shown in Fig. 4.1, the "left 333 km box radius" would refer to a 333 km X 666 km box on the left side of the cyclone, whose right side intersected the eye of the storm. Such will be the terminology used in this study.

The statistics were calculated for each left and right box radius (27.5 km, 55 km, 111 km, 222 km, 333 km, and 444 km) for each map time shown in Table 4.1. This was also done for two different frequencies: 85 GHz vertical polarization, (85V GHz) and 19 GHz horizontal polarization (19H GHz). Emphasis will be placed on 85 GHz because of its superior resolution and sensitivity to ice scattering in convective clouds (Glass and Felde, 1990 and Lee and Caughey, 1989).

As discussed in the previous chapter, two polarizations of these frequencies are available. The reason the 85 GHz vertical polarization was chosen over the horizontal, is because the former is less dependent on surface features than is horizontal polarization. Therefore, since scattering effects at 85 GHz are independent of

polarization, the vertical polarization will give more information about the atmosphere, rather than surface influences (Wilhiet et al., 1982).

Horizontal polarization for 19 GHz was used for the ability to determine the amount of ice versus rain present in the cyclones (Spencer and Hood, 1989). Since the 85V GHz measurements should react to the ice scattering in the thick rainband clouds, a relationship to the rain rate (and therefore cyclone intensity) can be determined. The 19H GHz channel can be used for comparison purposes, as will be shown in chapter V.

c. Brightness Temperature anomalies

The main emphasis of this study involved the use of the 85V GHz TB statistics in generating TB anomalies for comparison to storm traits. An anomaly is defined as the difference between the mean TB values, as calculated above, within two defined areas of box radii. TB anomalies (at 85V GHz) should highlight asymmetries of convection within tropical cyclones. As indicated in Chapter

II, earlier studies (for example, Kidder et al., 1978 and Gentry et al., 1980) found certain relationships between microwave measurements, anomalies, and cyclone intensity. The behavior of the 85V GHz TB anomaly should reflect the changes and distribution of the rain rates across the cyclone. Such anomalies in the Brightness Temperatures may reveal processes within the cyclone that affect traits such as intensity. An attempt was made to see if these anomalies were correlated to storm traits, and will be discussed shortly.

This research concentrated on two types of anomalies: 1) an "outer minus inner anomaly," and 2) a "right minus left anomaly." The first is defined as the mean TB in an inner box with a given radius, subtracted from the mean TB in an outer annulus. The annulus is defined as the area between the outer and inner boxes, and was calculated as follows:

$$TB \text{ annulus} = \frac{n_e TB_e - n_i TB_i}{n_e - n_i} \quad (6)$$

where,

n_e = number of TB values in the larger (or

exterior) box

n_i = number of TB values found in the smaller (or
inner box)

TB_e = mean TB in larger box

TB_i = mean TB in inner box

This type of anomaly (and associated annulus) was calculated on each side (right and left) of the cyclone, and oriented along the cyclone heading as shown in Fig. 4.1. Note that the annulus is actually one of rectangular shape rather than the conventional circle, but nevertheless, encompasses a portion of the rain band. Here, the annulus results from a series of concentric boxes rather than from concentric circles.

The second type of anomaly was simply defined as the difference in the mean TB's between the right and left boxes of equal radii (Fig. 4.1). The sign of the anomaly, in this case, reflects which side has cooler TB's, indicating the probable location of higher rain rates within a given radius. For example, a negative TB anomaly indicates a lower mean TB in the right box. Therefore, the left box

contains warmer TB values and relatively less rain. Refer to the appendix for further definitions of the terms used in this study.

d. *Analysis*

The final step involved analyzing comparisons between the TB data above, and the following storm traits:

(1) Future Intensity - defined as intensity (maximum sustained winds in kts) 24-hours after cyclone map time.

(2) Current Intensity - defined as intensity (maximum sustained winds in kts) at cyclone map time.

(3) Translation Speed - defined as translation speed (in kts) of the cyclone vortex between two successive fixes.

(4) Central Pressure Change - defined as the pressure change of the center of the cyclone (mb/hr)

24-hours after cyclone map time.

(5) Direction - defined as cyclone heading at map time.

The values for these traits were interpolated from the Annual Tropical Cyclone Reports for each map time, and loaded into a personal computer data base along with the associated statistical data (i.e., mean TB, TB anomaly, and variance). Through stratifying the TB statistics by cyclone trait, spreadsheets could be used to calculate correlation coefficients and graphically illustrate the relationships between TB data and cyclone trait.

Additionally, some stratifications were combined to introduce a second dimension into the analysis. Items (1) and (3), for example, were combined such that a correlation coefficient was calculated between an anomaly and future intensity, but only for those cyclones traveling at speeds < 6 kts. Similarly, items (1) and (5) were combined, analyzing only those map times where the direction was in the Northwest quadrant. Likewise, for item

(4), only map times where deepening occurred were considered, followed by filling incidences.

Within each stratification, the box radii were varied as shown in Table 4.2, and correlation coefficients were calculated for each combination of anomaly and storm trait. The correlation coefficients were calculated automatically within personal computer spreadsheets using the following formula:

$$r = \frac{N \sum XY - \sum X \sum Y}{(\sum X^2 - (\sum X)^2)^{1/2} (\sum Y^2 - (\sum Y)^2)^{1/2}} \quad (7)$$

where,

N = number of map times considered (up to 29)

X = trait data (e.g., maximum sustained wind speed)

Y = the statistic (e.g., a TB anomaly)

Analysis of the correlation coefficients, along with the rest of the TB statistics, was conducted to uncover any patterns that emerged from a particular data stratification. Case studies were also examined for cyclones that had an abundance of SSM/I data (i.e., at least five orbit passes). Such

Outer-Inner Anomaly	Right-Left Anomaly	Mean TB	Variance
right 444-333	444	right 444	right 444
left 444-333	333	left 444	left 444
right 444-222	222	right 333	right 333
left 444-222	111	left 333	left 333
right 444-111	55	right 222	right 222
left 444-111	27.5	left 222	left 222
right 444-55		right 111	right 111
left 444-55		left 111	left 111
right 444-27.5		right 55	right 55
left 444-27.5		left 55	left 55
right 333-222		right 27.5	right 27.5
left 333-222		left 27.5	left 27.5
right 333-111			
left 333-111			
right 333-55			
left 333-55			
right 333-27.5			
left 333-27.5			
right 222-111			
left 222-111			
right 222-55			
left 222-55			
right 222-27.5			
left 222-27.5			

Table 4.2. Variations in box radii (km) used in this study to generate anomalies and conduct statistical analyses. Note for the outer-inner column, the larger radius in each line indicates the outer boundary of the annulus (see text and appendix for definitions).

studies examined the changes in the TB patterns over the lifecycle of the storm.

As described above, the data analysis performed in this study was highly automated, providing accurate and consistent results. This is especially true since the data collected by the sensor is also very accurate, as discussed in the previous chapter. A great attempt was made to collect the largest data base feasible, and process it as uniformly as possible. However, data describing the cyclone traits is not as accurate as the TB data due to interpolation of the six-hourly, or sometimes twelve-hourly, storm observations. Moreover, the maximum sustained wind values were estimated using the Dvorak (1984) technique, which is not as precise as the TB measurements. Therefore, it should be noted that the correlations were calculated by comparing relatively accurate data to less precise information. The same problem was noted earlier by Rhudy (1989).

CHAPTER V. RESULTS

a. General

The underlying hypothesis behind this research was to determine if the SSM/I measured Brightness Temperatures revealed asymmetries in the cyclone, which could be related to traits such as intensity. As discussed in the previous chapter, the TB anomalies calculated from numerous combinations of box sizes and then correlated to storm characteristics, would hopefully highlight these asymmetries.

If high correlations exist between TB anomalies and storm traits, operational forecasting tools involving SSM/I microwave data may be developed. Findings from this research support the idea that SSM/I data, including TB anomalies, reveal certain characteristics of tropical cyclones that would otherwise not be evident from conventional (VIS/IR) satellite data. First, average TB's will be examined to gain an understanding of how they behave with intensity, and then the TB anomalies will be

studied in detail.

b. Mean Brightness Temperatures

Fig. 5.1 illustrates a decreasing 85 GHz vertical polarization (85V GHz) mean TB with increasing future intensity (maximum sustained winds 24 hours after the map time of the measured TB) for a left 55 km box. The correlation coefficient was -0.63. When only the cyclones traveling with a Northwest quadrant direction were considered (Fig. 5.2), the correlation improved to -0.81 for the same box radius. Similarly, Fig. 5.3 shows the 85V GHz mean TB in the left 27.5 km box for storms moving less than 6 kts (slow movers). A correlation of -0.83 was achieved. Fig. 5.4 shows the mean TB versus future intensity for the same box, but for the 19 GHz horizontal polarization (19H GHz) channel. Note the opposite reaction of 19H GHz to intensity.

These diagrams show that 85V GHz responds to the growing presence of scattering-causing, thick rainbands and ice crystals which are manifested by

AVERAGE TB's vs FUTURE INTENSITY IN THE LEFT 55 km BOX

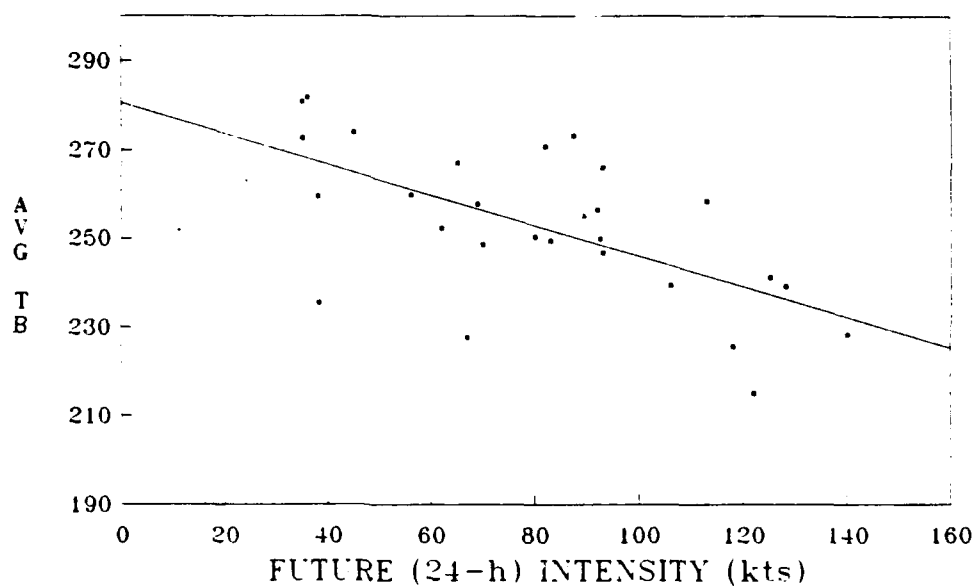


Fig. 5.1. Scatter diagram of future (24-h) maximum winds (kts) versus 85 GHz vertically polarized average Brightness Temperatures for the left 55 km box. Correlation coefficient, r , is -0.63.

AVERAGE TB's vs FUTURE INTENSITY AND NW DIRECTION IN THE LEFT 55 km BOX

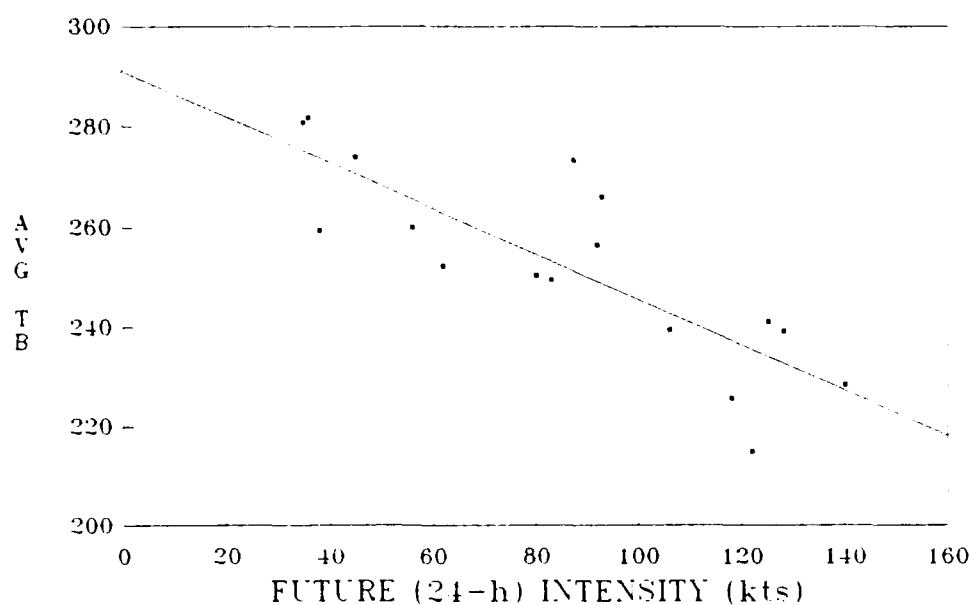


Fig. 5.2. As in Fig. 5.1 except only cyclones with a Northwest heading (i.e., in the Northwest quadrant) are considered ($r=-0.81$).

AVERAGE TB's vs FUTURE INTENSITY FOR
SLOW MOVERS IN THE LEFT 27.5 km BOX

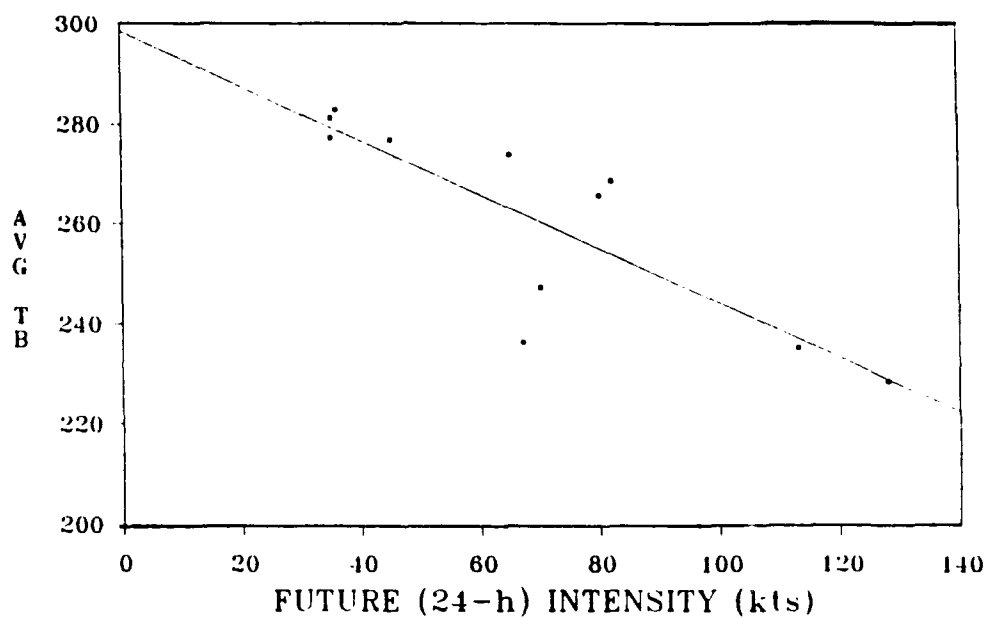


Fig. 5.3. Scatter diagram of future (24-h) maximum winds (kts) versus 85 GHz vertically polarized average Brightness Temperatures for the left 27.5 km box. Only cyclones traveling < 6 kts are considered ($r=-0.83$).

AVERAGE TB's vs FUTURE INTENSITY IN THE LEFT 27.5 km BOX

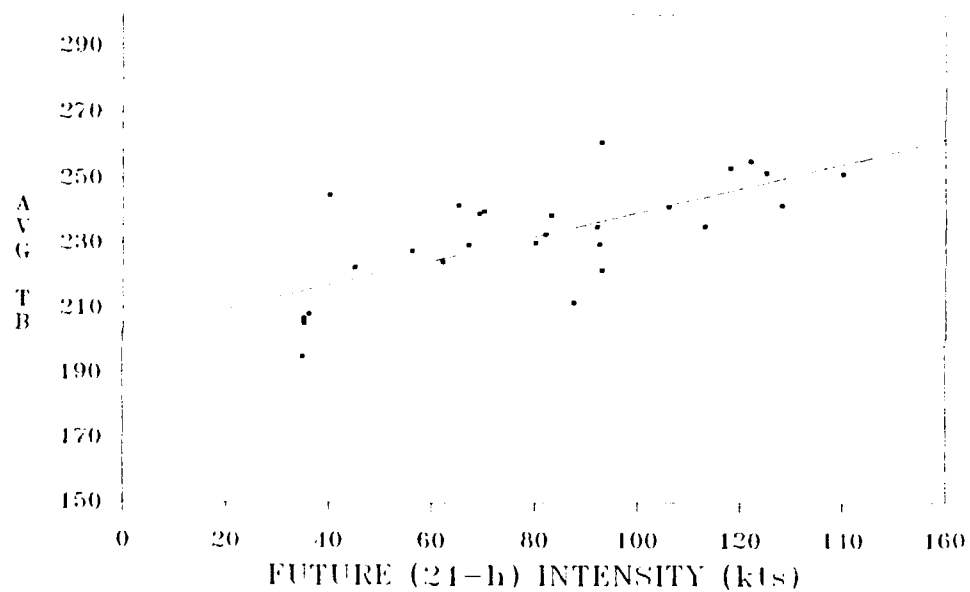


Fig. 5.4. Scatter diagram of future (24-h) maximum winds (kts) versus 19 GHz horizontally polarized average Brightness Temperatures for the left 27.5 km box ($r=0.67$).

rising convection and increasing rain rates. The cooler 85V GHz (and warmer 19H GHz) values resulting from such phenomenon was discussed in Chapter III. Through the use of Spencer and Hood's (1989) diagram, shown in Fig. 5.5, an analysis of 85 and 19 GHz TB's determined some of the typhoons to have ice present in the inner most box radii (see Table 5.1). Fig. 5.5 also demonstrates the inverse behavior of the 19 and 85 GHz channels, as discussed in Chapter III.

For the 85V GHz mean TB's, it was found that higher correlations (against current and future intensity) consistently appeared on the left side for boxes less than 111 km in radius. For radii 111 km and larger, the higher correlations switched to the right side. The highest correlations, however, were always with the smaller boxes (< 111 km), on the left side. The left side also demonstrated better slopes as well.

The physical explanation for this can be understood by examining Fig. 5.6, which is VIS imagery of Typhoon Wynne at 2015 UTC on 25 July

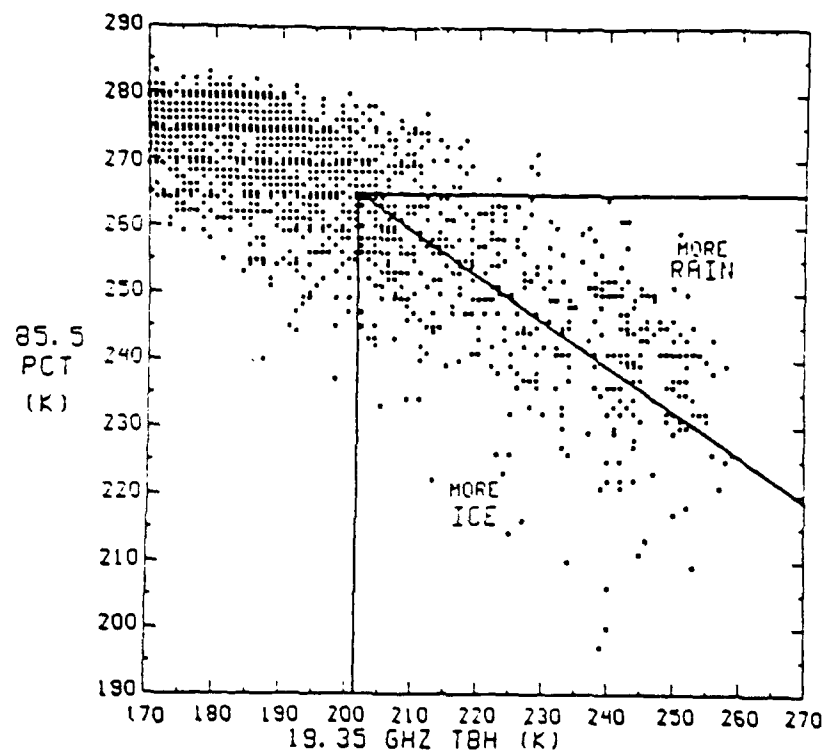


Fig. 5.5. Scatter diagram showing relationship between rain and ice signals (19.35H GHz vs 85.5 GHz) for Tropical Storm Greg (after Spencer and Hood, 1989)

CYCLONE (ORBIT)	LOWEST 85V GHz TB	LOCATION	CORRESPONDING 19H GHz TB
CARY (788)	227 K	55 km (left)	236 K
DINAH (936)	207 K	27.5 km (left)	255 K
FREDA (1106)	223 K	55 km (right)	248 K
HOLLY (1147)	228 K	27.5 km (left)	242 K
HOLLY (1161)	235 K	27.5 km (left)	235 K
NINA (2200)	232 K	111 km (left)	238 K
VERNON (428)	231 K	27.5 km (right)	225 K
WYNNE (505)	213 K	27.5 km (right)	257 K

Table 5.1. Cyclone map times with ice hydrometeors as determined by Spencer and Hood (1989) methodology (see Fig. 5.5). Note: Typhoons Alex (506) and Lynn (1692, 1698, and 1712) had values on the diagonal line.

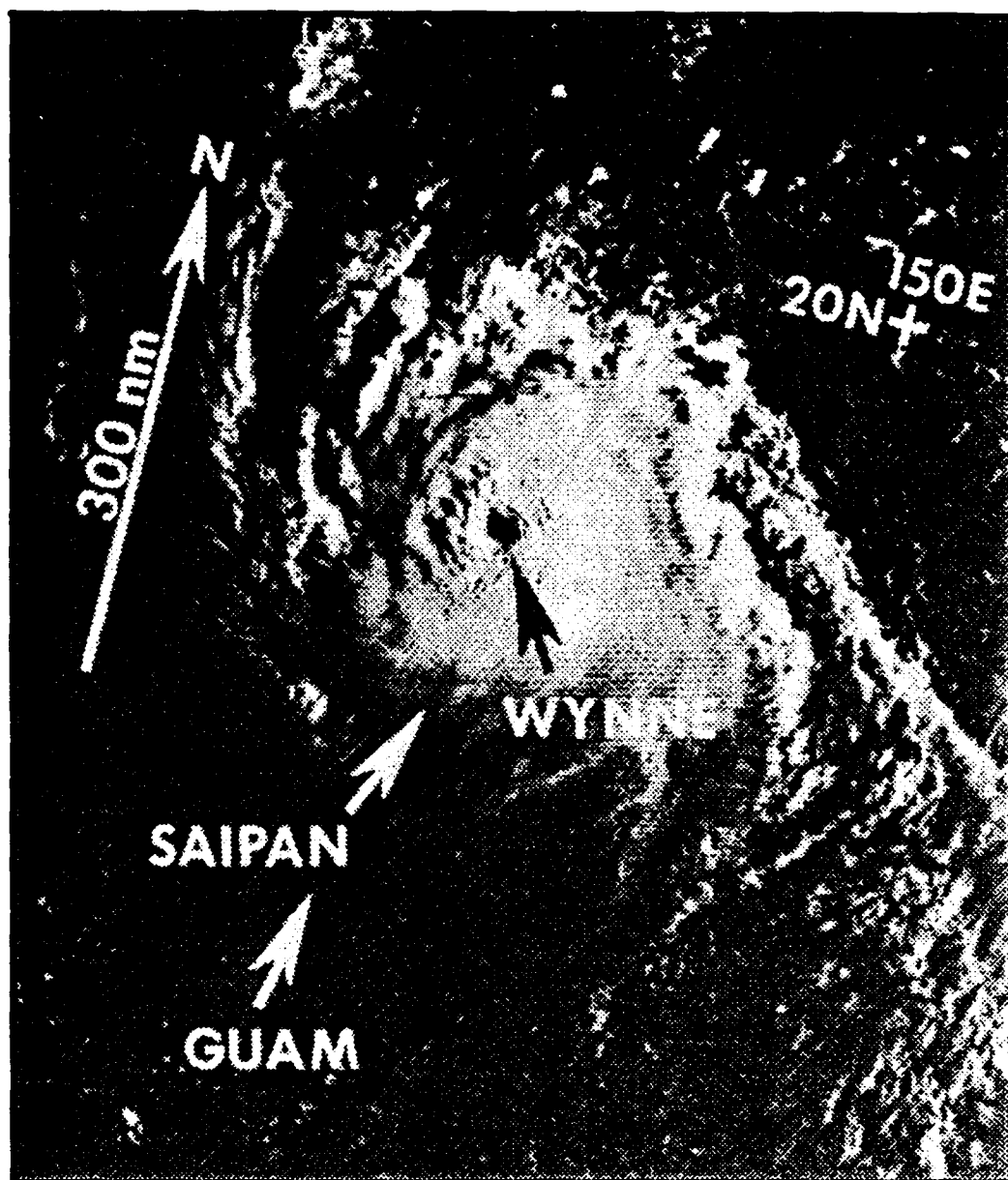


Fig. 5.6. Visible imagery of Typhoon Wynne at 2015 UTC on 25 July 1987, which is approximately the same map time used in this study (after Hoffman et al., 1987).

1987. The higher clouds of the principle rainband can clearly be seen on the left side (with respect to direction of motion, 292 degrees) relatively near the eye. On the right side, however, the rainband extends further out from the eye. Thus it is apparent that the correlations of the SSM/I TB's are revealing the physical processes responsible for the intensity. Figs. 5.7 and 5.8 portray similar patterns in the VIS and radar depictions of Typhoon Vernon. The same pattern occurred for the TB anomalies as well and will be discussed later.

Correlations using TB variance were also calculated in this study. Only three correlations exceeded 0.50 with variance for all box sizes across the data stratification. Figs. 5.9 and 5.10 illustrate two of them, and reveal a similar pattern in the scatter diagram as described above. The right 333 km box gave a correlation of 0.58 (Fig. 5.9), while the left 55 km box gave 0.59. The remainder of the correlations were very poor, except for the left 333 km box, which gave 0.52 (not shown). These diagrams seem to support the pattern described above, as variance is a measure of the

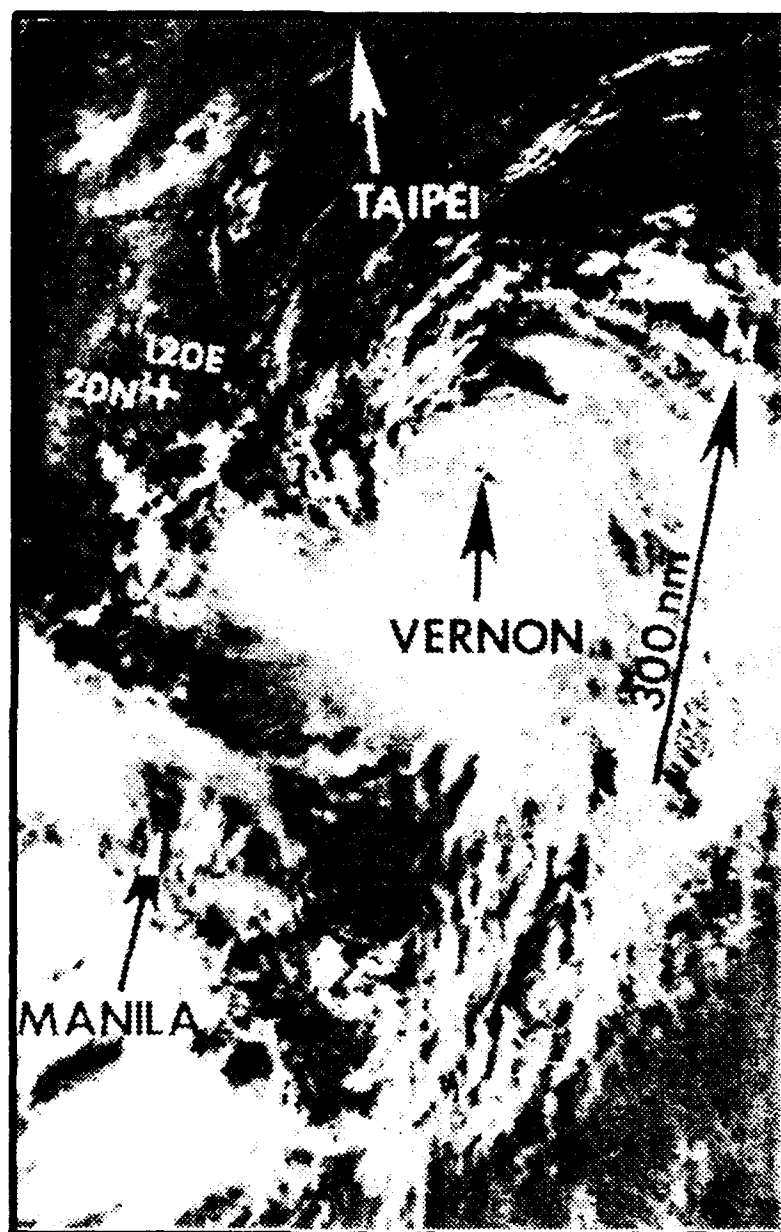


Fig. 5.7. Visible imagery of Typhoon Vernon at 0143 UTC on 20 August 1987 (after Hoffman et al., 1987).

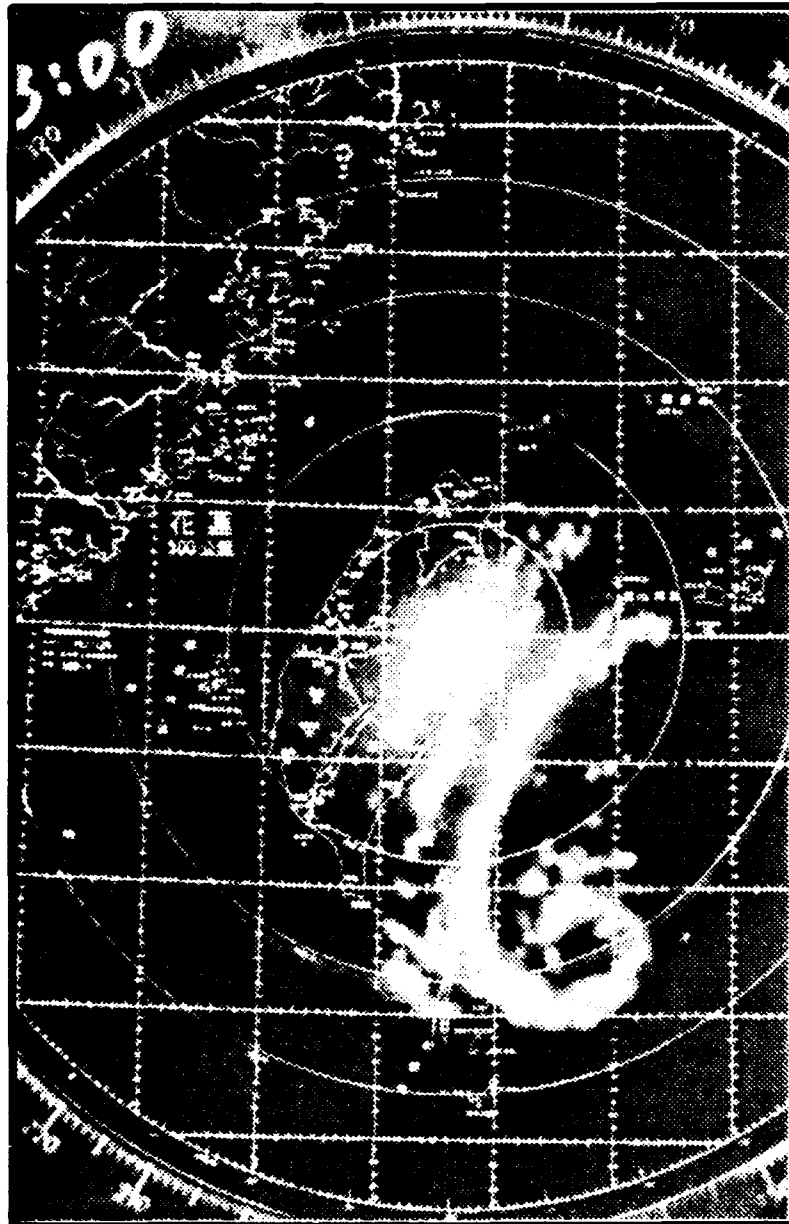


Fig. 5.8. Radar imagery of Typhoon Vernon at 1500 UTC on 20 August 1987 (after Hoffman et al., 1987).

TB VARIANCE vs FUTURE INTENSITY IN THE
RIGHT 333 km BOX FOR SLOW MOVERS

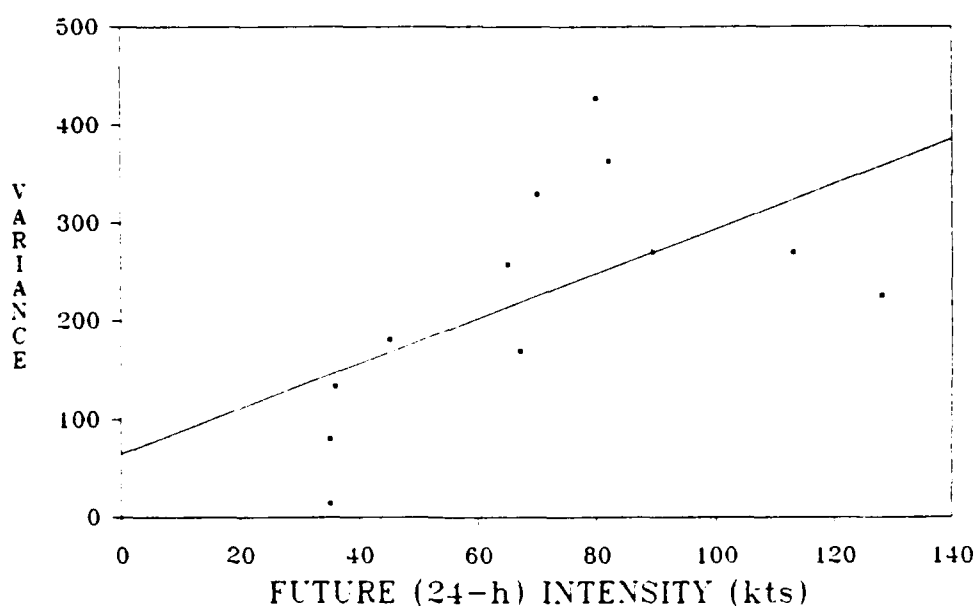


Fig. 5.9. Scatter diagram of future (24-h) maximum winds (kts) versus 85 GHz vertically polarized Brightness Temperature variance for the right 333 km box. Only cyclones traveling <6 kts are depicted ($r=0.58$).

TB VARIANCE vs FUTURE INTENSITY
IN THE LEFT 55 km BOX FOR CYCLONES
WITH NORTHWEST HEADINGS

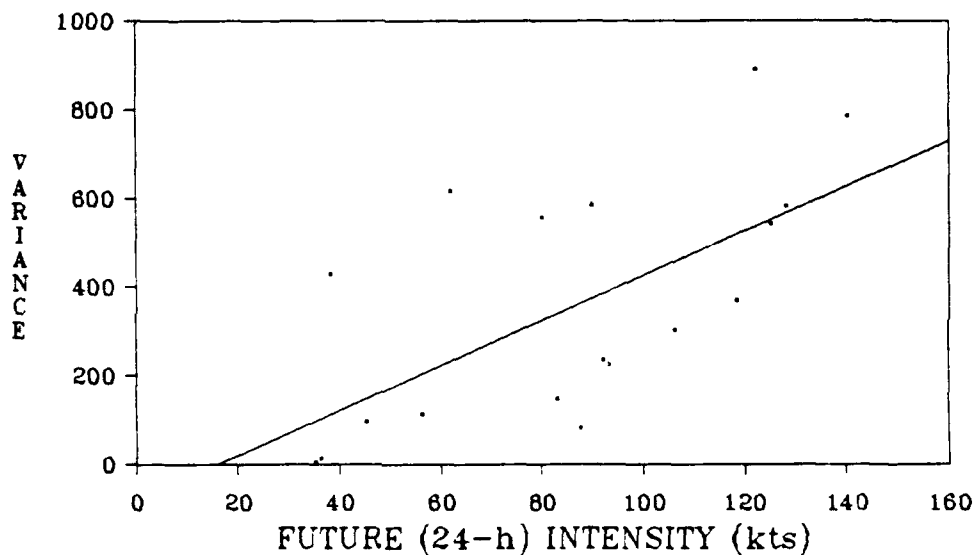


Fig. 5.10. Scatter diagram of future (24-h) maximum winds (kts) versus 85 GHz vertically polarized TB variance for the left 55 km box. Only cyclones traveling in a northwesterly direction are depicted ($r=0.59$).

spread of maximum and minimum TB values. It is reasonable for such a spread to increase with intensity, as Figs. 5.9 and 5.10 show. It is interesting that the best correlations were obtained at the radii described. The anomalies further support this phenomena.

c. Brightness Temperature anomalies

In general, it was found that for the 29 map times of typhoon cases, as intensity increased so did the TB anomaly. This was true for nearly all anomaly versus maximum wind and translation speed cases, and is an expected result since a large temperature gradient indicates an intense system. When anomalies were compared to filling rates, however, negative correlations were found. The reason for this will be discussed later in this chapter.

The increasing TB anomalies portray increasing asymmetries of convection in the spiral rainbands as a storm intensifies (Lee and Caughey, 1989). The specific signatures that resulted from analyzing the

two basic types of 85 GHz TB anomalies (the "outer annulus-inner box anomaly", and the "right-left anomaly") will be discussed.

(1) *Outer-inner anomalies*

The outer-inner type anomaly portrays the relationship between the interior part of the cyclone and its outer environment. For this type of anomaly, similar patterns of high correlations emerged as was found with the average TB's. Fig. 5.11, for example, shows the scatter diagram of TB anomaly versus future intensity. Here, the anomaly is defined as the mean 85V GHz TB in a 444 km annulus on the right side, minus the mean 85V GHz TB in the right 222 km box. A correlation of 0.55 was achieved, which was one of the best correlations of the outer-inner type anomalies. The corresponding correlation on the left was only 0.31 (not shown).

As will be presented later, the other high correlations occurred on the left side with smaller inner boxes, fitting the pattern described above. The largest anomalies, as high as 58.37 K, also

TB ANOMALY vs FUTURE INTENSITY

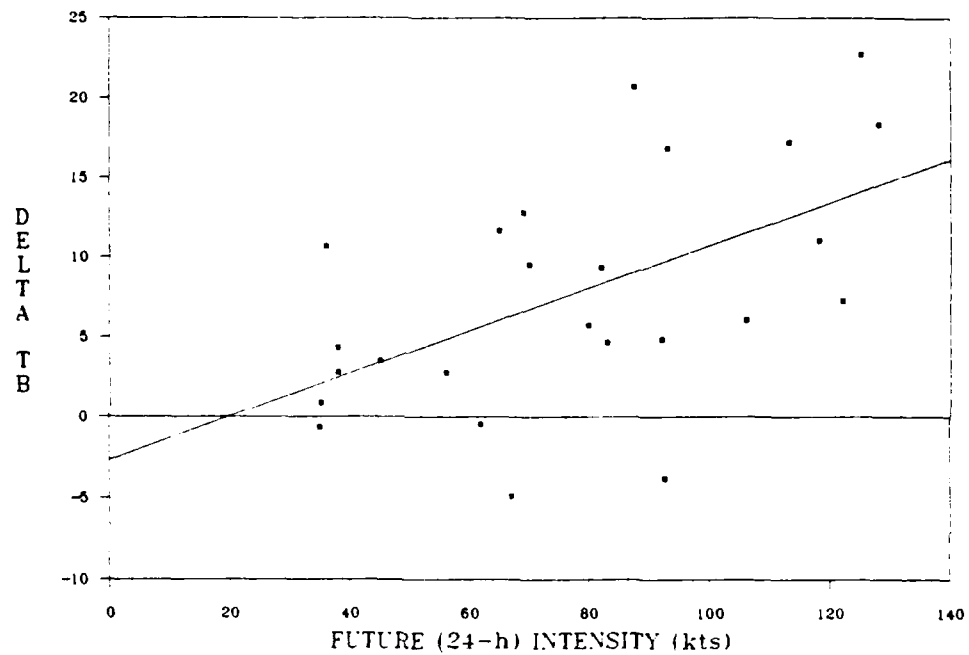


Fig. 5.11. Scatter diagram of future (24-h) maximum winds (kts) versus 85 GHz vertically polarized TB anomaly for a right 444 km annulus and the right 222 km interior box ($r=0.55$).

tended to occur on the left for smaller interior boxes. Most other anomalies for interior boxes greater than 111 km, averaged closer to 10.0 K.

The predominance of positive anomaly values, found mostly at higher intensities, indicate warmer outer regions and cooler inner regions of the cyclones. This suggests the heaviest rain rates and largest amounts of ice hydrometeors are either in the inner portions of the principal band or eyewall region. Points with negative TB anomalies indicate cyclones with warm inner boxes.

The reason for this is the location of the spiral rainbands the 85V GHz channel is sensing. If the inner box is warmer, the rainband is outside the radius of the inner box. Indeed, more negative points were encountered as the inner box was reduced in size, indicating a position of the rainband beyond the radius in question. The warm 85V GHz TB values near the eye also cause an increase in negative values for smaller interior box radii. The greater number of negative anomalies for less intense storms probably indicates the fact that

concentric eyewalls had not moved inward yet, as discussed by Rodgers and Adler (1981). In many cases, the location of the principal rainband is apparent just by examining the positive and negative TB anomalies.

Moreover, some rainbands rotate while others are stationary (Willoughby, 1988). Calculating the absolute value for the anomaly would then take into account the varied position of the rainband. Slightly higher correlations were achieved when this was accomplished. For example, with the same TB definition as in Fig. 5.11, the correlation rose to 0.61 when the absolute value was taken. Therefore, the 85V GHz TB data are affected by the location of the principal rainband. Similarly, Adler et al. (1990) found higher microwave frequencies (near 92 GHz) to depict rain boundaries rather well.

An understanding of why a pattern of higher correlations on the right for larger interior boxes, versus higher values on the left for smaller inner boxes, now becomes apparent. In many of the cyclones used in this study, the rainband spiraled

outward from the inner left side of the cyclone (with respect to direction) to the outer portions on the right. Thus, the best correlations for intensity occurred where the 85V GHz anomalies were calculated in the vicinity of the principal rainband (and, therefore, the largest rain rates).

This was not the case, however, for the corresponding 19H GHz measurements. The 19H GHz TB anomalies indicated negative correlations across all stratifications of the data. Fig. 5.12 shows a correlation of -0.51 for the 19H GHz TB anomaly of a right 444 km annulus and a right 222 km interior box. Note the opposite slope as compared to Fig. 5.11. The reason for this, as discussed in Chapter III, is the sensing of lower levels in the atmosphere. Therefore, warmer inner boxes always result, depicting the greater emissions (possibly due to extremely rough seas and sea foam) within the bounds of the cyclone. When the absolute value is taken, the correlations fall instead of improve, indicating that 19H GHz is not sensing the rainbands, but features underneath.

TB ANOMALY vs FUTURE INTENSITY

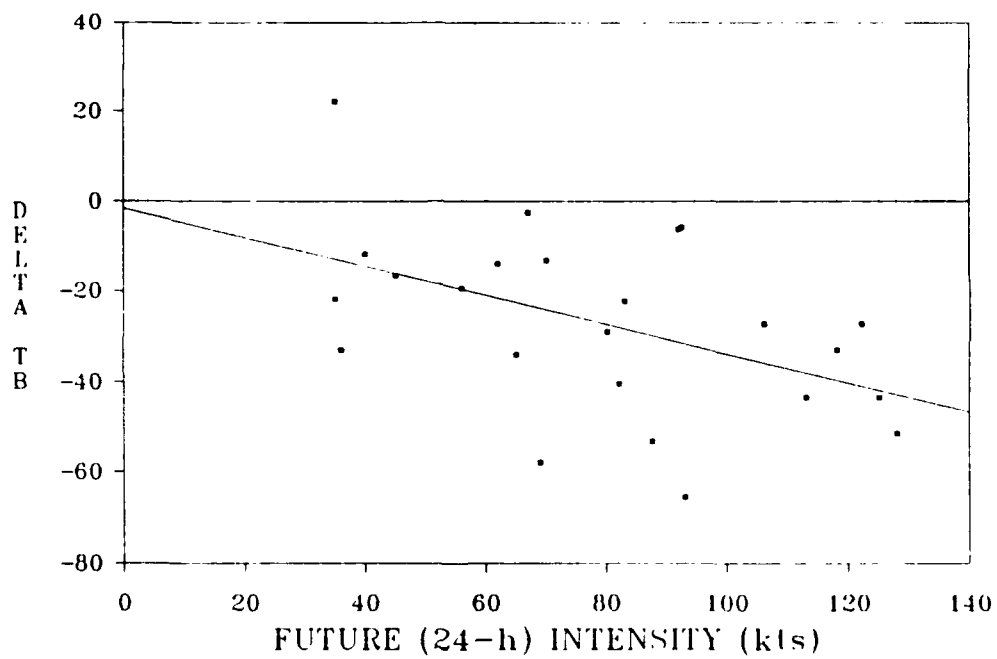


Fig. 5.12: As in Fig. 5.11, except for 19 GHz horizontally polarized TB ($r=-0.51$).

Other stratifications were used in the anomaly analysis as well. Keeping with the same box parameters (444 km annulus versus 222 km box), but this time examining only slow movers, the future intensity correlation became 0.69 (Fig. 5.13) and 0.82 for the absolute value. Fig. 5.14 shows the same parameters but for a larger (333 km) interior box. The correlation was 0.82 with, and without the absolute value (there were no negative data points). Similarly, but for the 19H GHz channel and for the left side, the correlation was -0.77 (Fig. 5.15).

It was noted that most cyclones used in this study seemed to slow down significantly approximately 12-24 hours prior to maximum intensity. Then, as the cyclone began to subside, the vortex translation speed increased. It was for this reason that this "third-level" stratification was examined. These improved correlations can best be explained by drawing attention to the fact that there is a better relationship when storms with similar traits are compared. Fig. 5.16 further illustrates this point. The parameters are the same as above, but only storms traveling in a Northwest

TB ANOMALY vs FUTURE INTENSITY FOR SLOW MOVERS

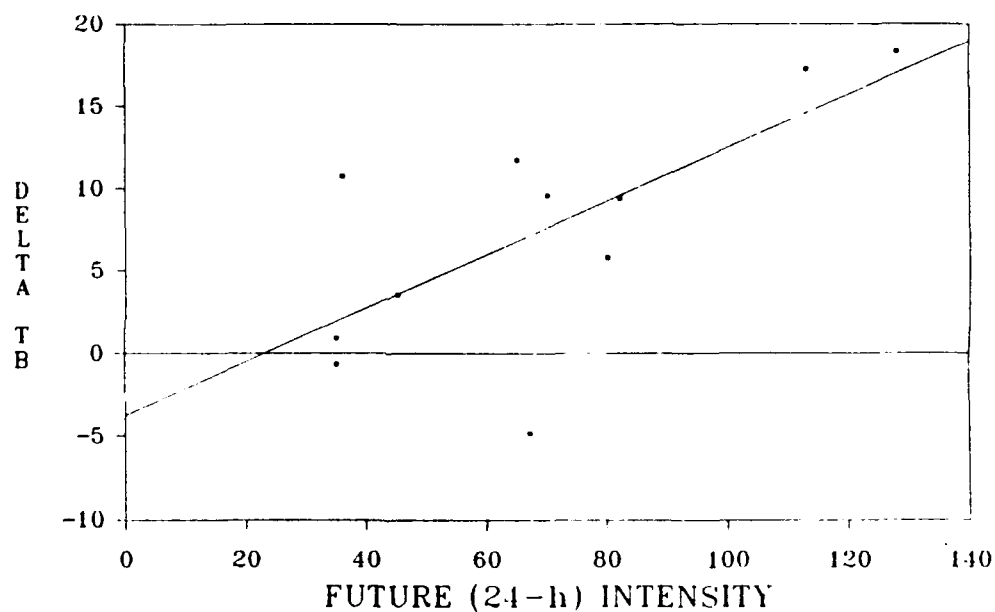


Fig. 5.13. As in Fig. 5.11, except for cyclones traveling < 6 kts only. Note the resulting improvement in correlation, $r=0.69$.

TB ANOMALY vs FUTURE INTENSITY FOR SLOW MOVERS

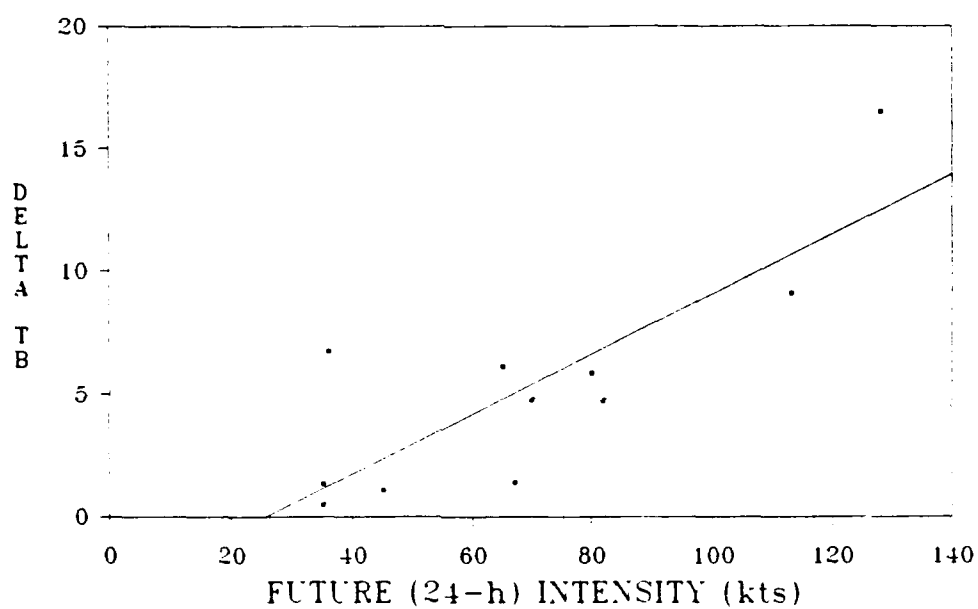


Fig. 5.14. Scatter diagram of future (24-h) maximum winds (kts) versus 85 GHz vertically polarized TB anomaly for a right 444 km annulus and the right 333 km interior box. Only cyclones traveling <6 kts are considered ($r=0.82$).

TB ANOMALY vs FUTURE INTENSITY FOR SLOW MOVERS

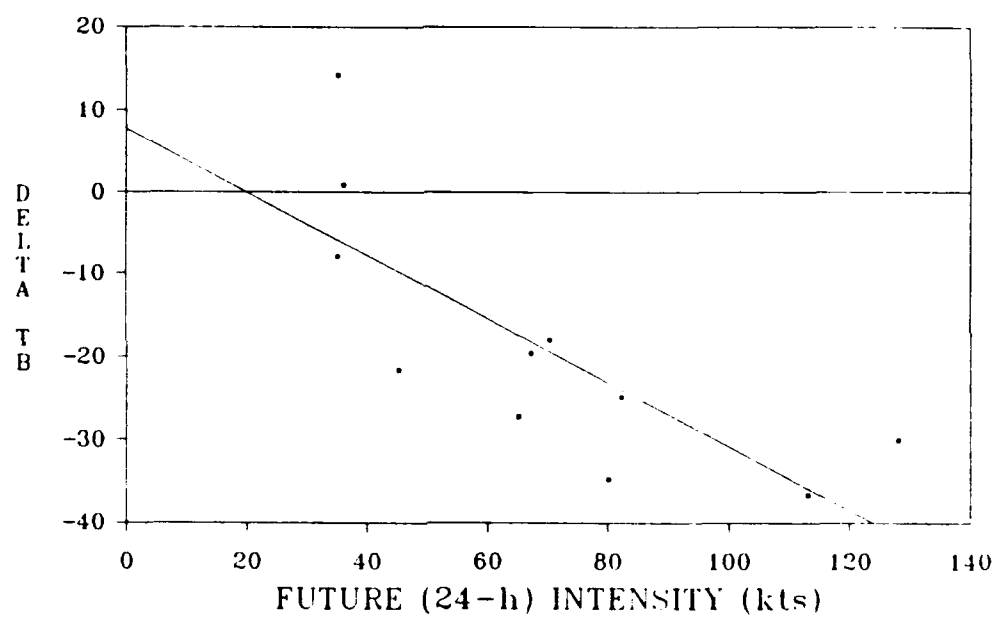


Fig. 5.15. As in Fig. 5.14, except for 19 GHz horizontal polarization and anomaly taken on the left side ($r = -0.77$).

TB ANOMALY vs FUTURE INTENSITY FOR CYCLONES WITH NORTHWEST HEADINGS

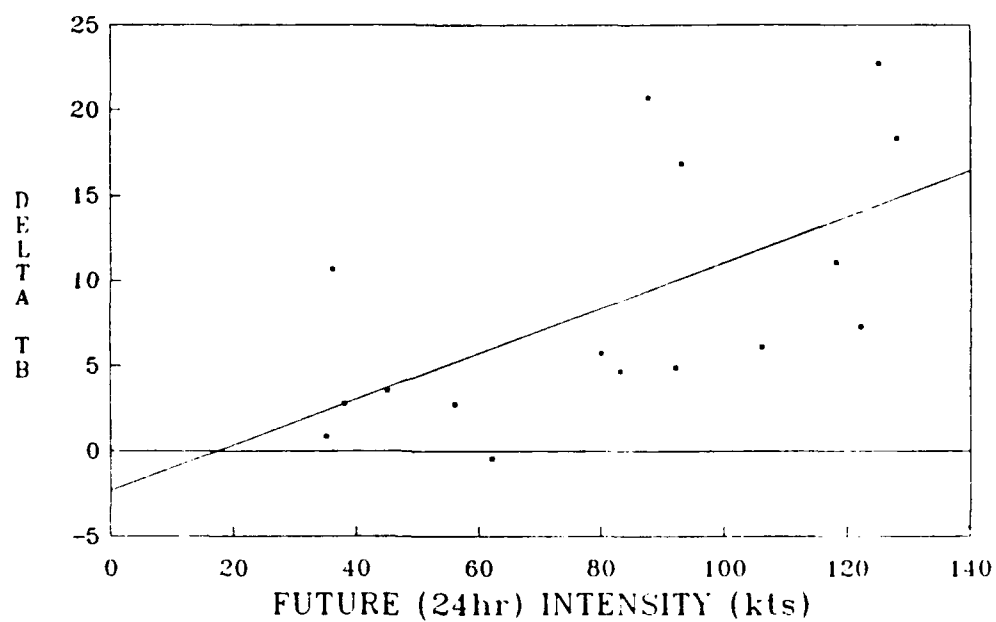


Fig. 5.16. As in Fig. 5.11, except for cyclones traveling in a northwesterly direction ($r=0.61$).

direction are considered. Again, a better correlation is achieved (0.61) than with all map times of future intensity.

It should be noted again, however, that Fiorino and Elsberry (1989) found translation speed and direction of motion to be related to the strength of the flow in the outer portions of a cyclone. Burpee and Black (1989) also found translation speed to be one of the factors influencing the asymmetrical precipitation patterns in the eyewall, which may relate to intensity change. These factors may be influencing the SSM/I data.

Continuing with the illustration of right versus left patterns, figs. 5.17 through 5.22 examine left side TB anomalies with inner boxes 55 km and less. Fig. 5.17 shows a left 444 km annulus and a left 55 km interior box. This TB anomaly versus future intensity gave a 0.52 correlation. The corresponding right side correlation was only 0.34 (not shown). Fig. 5.18 illustrates a scatter diagram using the same parameters but for Northwest traveling storms, giving a correlation of 0.77. The

TB ANOMALY vs FUTURE INTENSITY

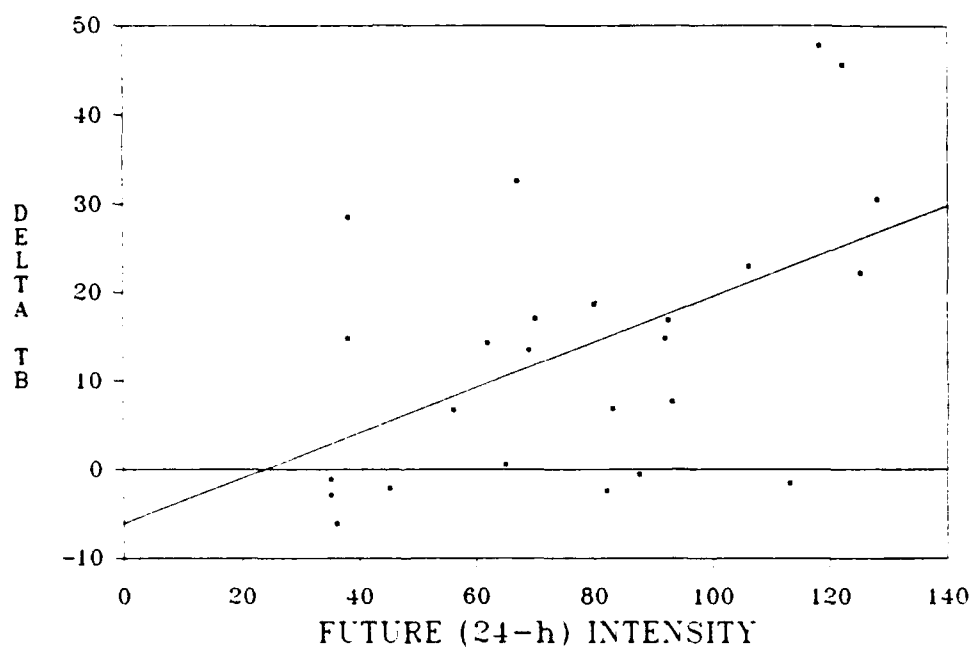


Fig. 5.17. Scatter diagram of future (24-h) maximum winds (kts) versus 85 GHz vertically polarized TB anomaly for a left 444 km annulus and the left 55 km interior box ($r=0.52$).

TB ANOMALY vs FUTURE INTENSITY FOR CYCLONES WITH NORTHWEST HEADINGS

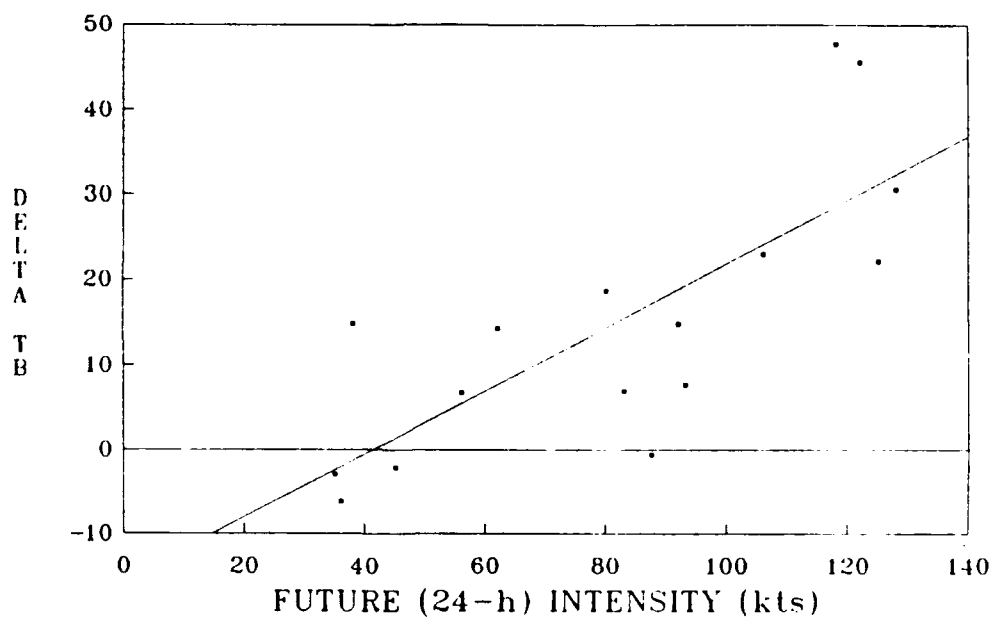


Fig. 5.18. As in Fig. 5.17, except for cyclones traveling in a northwesterly direction only ($r=0.77$). Note the improvement in correlation.

TB ANOMALY vs FUTURE INTENSITY FOR CYCLONES WITH NORHTWEST HEADINGS

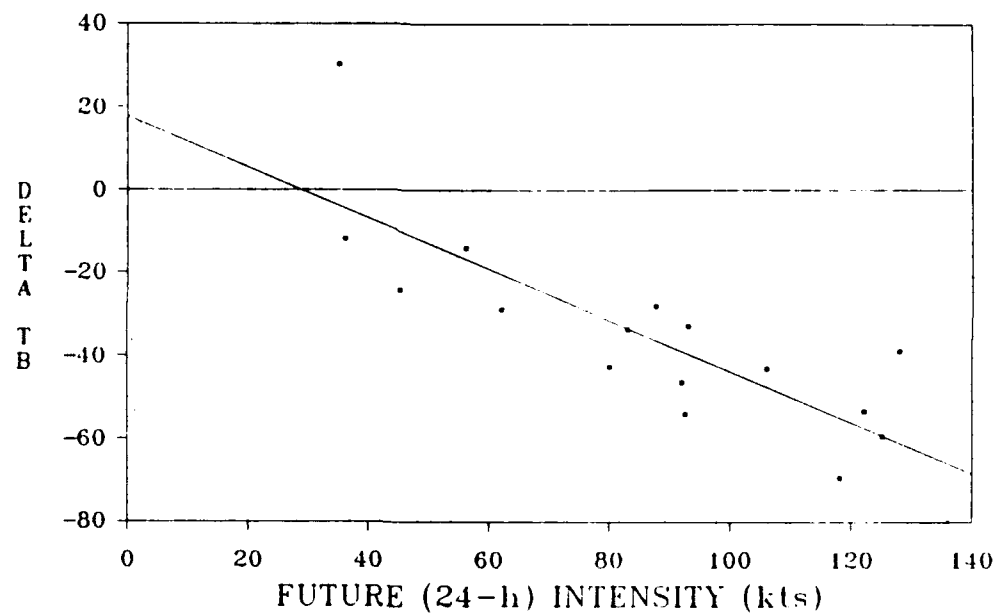


Fig. 5.19. As in Fig. 5.18, except for 19 GHz horizontal polarization ($r=-0.75$).

TB ANOMALY vs FUTURE INTENSITY FOR SLOW MOVERS

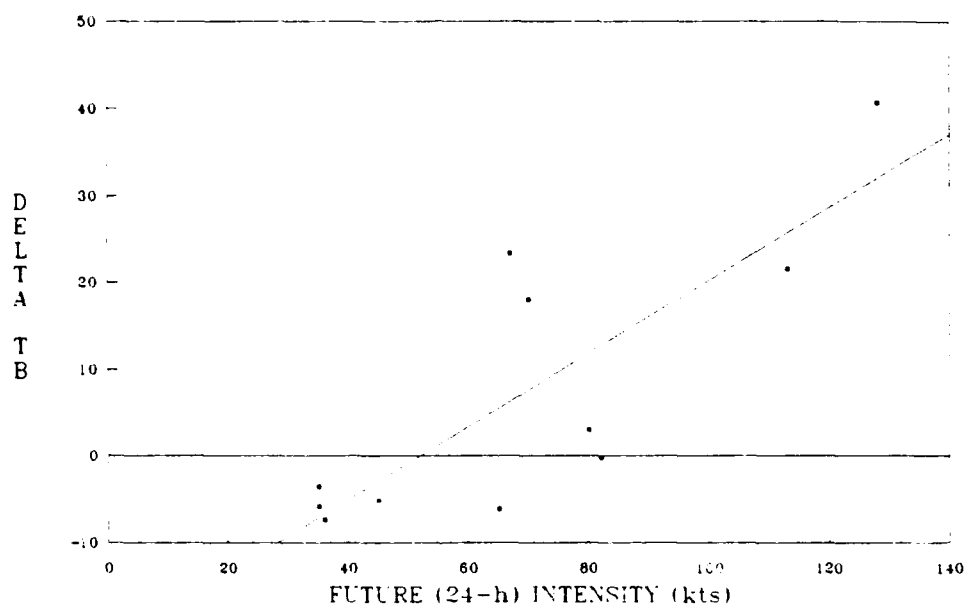


Fig. 5.20. Scatter diagram of future (24-h) maximum winds (kts) versus 85 GHz vertically polarized TB anomaly for a left 444 km annulus and the left 27.5 km interior box. Only cyclones traveling <6 kts are considered ($r=0.81$).

TB ANOMALY vs FUTURE INTENSITY

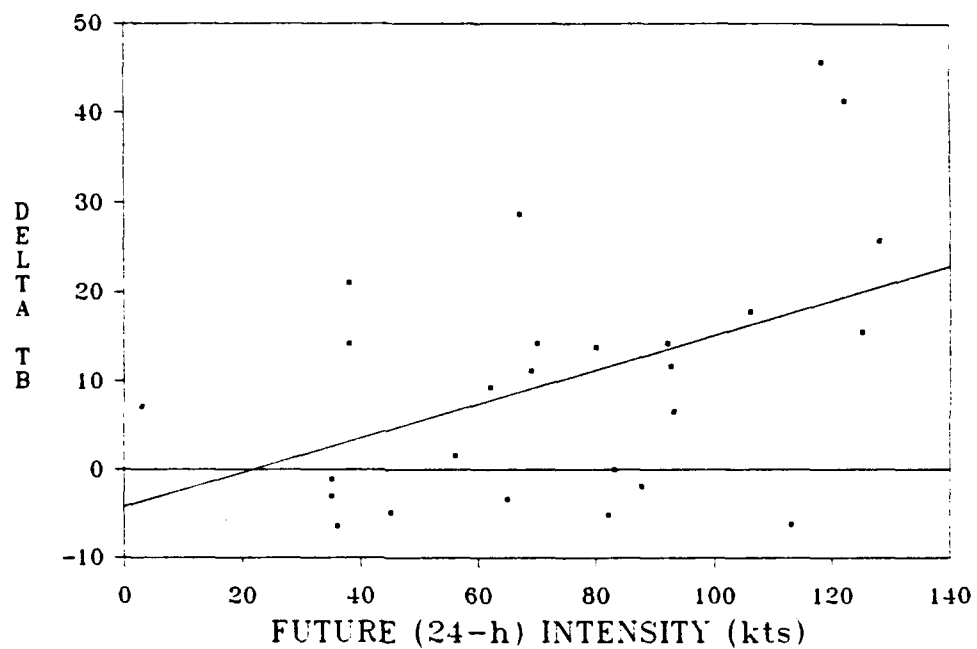


Fig. 5.21. Scatter diagram of future (24-h) maximum winds (kts) versus 85 GHz vertically polarized TB anomaly for a left 333 km annulus and the left 55 km interior box ($r=0.48$).

TB ANOMALY vs FUTURE INTENSITY FOR SLOW MOVERS

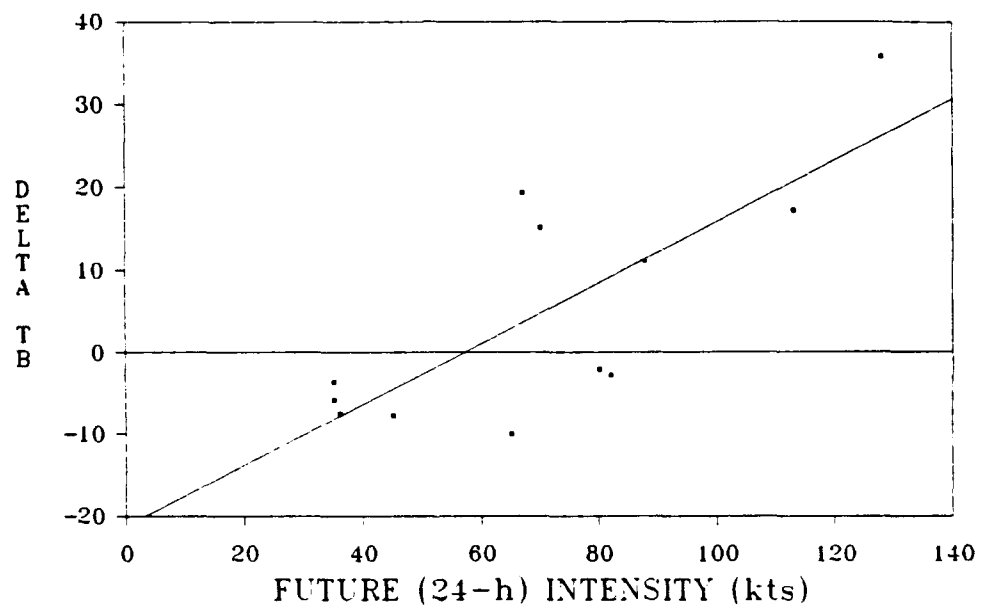


Fig. 5.22. Scatter diagram of future (24-h) maximum winds (kts) versus 85 GHz vertically polarized TB anomaly for a left 333 km annulus and the left 27.5 km interior box. Only cyclones traveling <6 kts are considered ($r=0.77$).

right side in this case gave only 0.46. The 19H GHz scatter diagram (for the left side) is shown in Fig. 5.19 for comparison. Here, the correlation was -0.75. The inner box was further reduced to 27.5 km for Fig. 5.20. In this case, only slow movers were examined, and the correlation was 0.81. The right side gave 0.29, a dramatic difference.

In addition to the inner box, the outer annulus was also reduced in an effort to see what correlations would result. The findings were the same for 333 km and 222 km outer annuli, as the 444 km annulus used above. Fig. 5.21 shows a TB anomaly defined with a left 333 km annulus and a left 55 km inner box versus future intensity. The correlation was 0.48. The correlation improved to 0.52 for slow movers, and 0.73 for Northwest traveling cyclones. The right side gave correlations of only 0.26, -0.07, and 0.38 respectively. Fig. 5.22 shows a correlation of 0.77 achieved with a left 27.5 km box and slow movers.

Until now, emphasis has been placed on data stratifications surrounding intensity simply because

they gave the most interesting results. However, several other types of storm traits were examined. Twenty four hour central pressure changes were examined to see how TB anomalies were effected. Only two correlations reached as high as 0.50, both occurring on the left side with inner boxes set at 55 km. The difference between these two was one had the outer annulus fixed at 444 km, and the other at 333 km.

When only deepening cyclones were considered, another pattern emerged. The highest correlations were on the right side for 111 km and 222 km interior boxes (the outer annuli were varied from 444 km to 222 km). The correlations were near 0.50, with the best at 0.60 as shown in Fig. 5.23. Virtually all of the remaining correlations for deepening rates were below 0.25, highlighting a definite pattern.

When filling rates were examined, the highest correlations followed a consistent pattern, and all had negative slopes. Fig. 5.24 illustrates a delta TB defined by a 444 km left annulus and a left 333

TB ANOMALY vs CENTRAL PRESSURE DEEPENING RATE

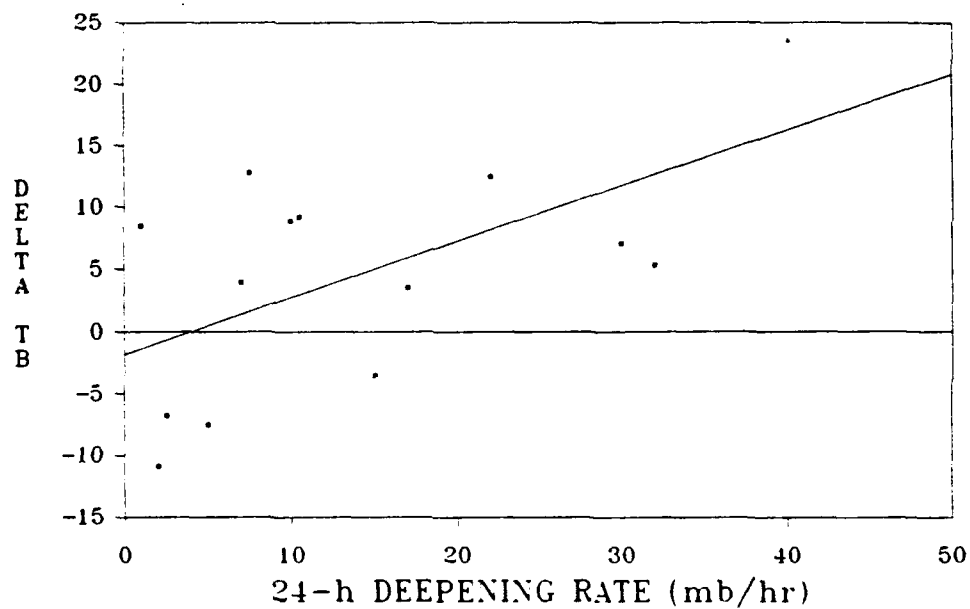


Fig. 5.23. Scatter diagram of future (24-h) central pressure change (mb/hr) versus 85 GHz vertically polarized TB anomaly for a right 333 km annulus and the right 222 km interior box. Only deepening cyclones are considered ($r=0.60$).

TB ANOMALY vs CENTRAL PRESSURE FILLING RATE

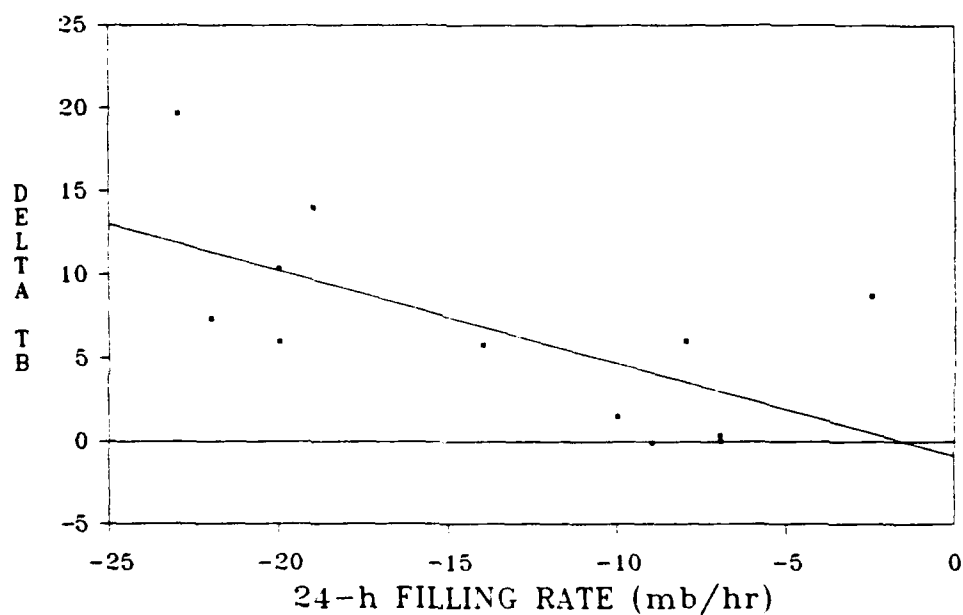


Fig. 5.24. Scatter diagram of future (24-h) central pressure change (mb/hr) versus 85 GHz vertically polarized TB anomaly for a left 444 km annulus and the left 333 km interior box. Only filling cyclones are considered ($r=-0.65$).

km inner box. The correlation was -0.65 . The reason for such negative correlations may be due to a more symmetric orientation of the rain bands. As Willoughby et al. (1984) and Willoughby (1988) discuss, the principal rain band acts as an asymptote, separating the interior flow from the outer environment. As it pulls inward and encircles the eye, the storm dissipates. Therefore, the storms filling the fastest (larger negative numbers) may have stronger barriers of thick, non-ice rainbands providing warm 85V GHz TB's. Indeed, the cyclones filling the fastest did not seem to have ice present. The better correlations shift to the right for inner boxes of 111 and 55 km, and then back to the left for inner boxes of 27.5 km. This illustrates the varying position of the spiraling band.

Vortex translation speed was also examined, and depicted a similar pattern to that of 24-h deepening, but with the best correlations on the left rather than the right (not shown). Correlations near 0.50 were found at each combination of left side TB definitions when the

inner box was fixed at 111 km. The highest value achieved for example, was 0.58 for a left 222 km annulus and a left 111 km box.

This seems to support the idea of translation speed being linked to the outer portions of a cyclone as discussed above. Moreover, both translation speed correlations and 24-h deepening correlations achieved the highest values beyond a certain radius: between 111 km and 222 km. This is apparently related to the effective radius as discussed by Holland (1983).

Another interesting feature of the translation speed calculations, was that slower moving storms (i.e., < 6 kts) seemed to have warmer TB's in the smaller box radii, than did the faster moving cyclones. For example, the average TB in the left 27.5 km box for slow moving cyclones was 261 K. For cyclones traveling > 14 kts, the average TB in the same box was 248 K, indicating the presence of a more well defined eye for map times closer to maximum intensity. Rhudy (1989) showed the usefulness of the 85V GHz data in locating the warm

eye of a cyclone. The case study of Lynn, later in this chapter, will show similar results.

Current intensity was another storm characteristic examined. Both Gentry et al. (1980) and Rhudy (1989) achieved higher correlations when comparisons of Brightness Temperatures were made against future intensity rather than current intensity. This study supports this finding, which was why earlier emphasis was placed on future intensity. Such predictive value embodied in the TB data seems to relate to the lag of intensity change to latent heat release change (Roders and Adler, 1981). However, with the larger data base and more combinations of anomalies, this study found a few cases where future intensity correlations did not exceed current.

Interestingly, future intensity correlations were better than current intensity for all box size combinations, except when the inner box was fixed at 27.5 km on the left side (with varying outer annuli). For example, for the anomaly defined with a left 444 km annulus minus the left 27.5 km box,

the correlation was 0.52 for current intensity and 0.44 for future intensity. The highest correlation in the future intensity stratification occurred with the inner box set at 222 km, suggesting this as the radius offering the optimum intensity predictability. However, this pattern did not hold for the other stratifications described in section d of chapter IV. Since the slow mover stratification portrayed better correlations with a 27.5 km inner box, translation speed affects may be more important in these interior regions, as discussed in Chapter II.

(2) *Right-left anomalies*

Preliminary work suggested that TB anomalies, generated by the difference in mean TB's between right and left boxes, would be well correlated to intensity and other characteristics, especially at the 111 km box radius (Rao et al., 1990). Since significant asymmetries in precipitation are often shown in tropical cyclones, as discussed in the previous chapter, it seems reasonable to expect a difference in the TB fields between the left and

right sides of a cyclone.

The outer-inner anomalies, however, gave better results. This may be due to changes experienced by a storm (intensity, for example) being linked to the rainband structure, rather than physical processes occurring only on each half of a storm. Outer-inner anomalies may be better able to discern this structure than can right-left anomalies.

There were few good correlations across the several stratifications of the data for the various right-left anomalies. In fact, the only good correlations came at the 27.5 km radius for future intensity with slow moving cyclones, and the 24-h filling rate. For the slow movers, the correlation was 0.51 with, and without the absolute value taken. As with the outer-inner anomalies, the delta TB's increased with increasing intensity. For the filling rate stratification, correlations of -0.53 and -0.55 were achieved with, and without the absolute value, respectively. Here, the negative correlation is believed to be due to the same phenomena in the outer-inner anomaly versus filling

rate discussion. The remainder of the correlations averaged near 0.10.

An examination of the actual TB anomaly values revealed some interesting results. There were more occurrences of large TB anomaly values in the 27.5 km radius for intense storms than for less intense storms (see Fig. 5.25). A small secondary maximum occurred at 111 km for the cyclones with winds greater than 90 kts. For weaker storms, the largest anomalies were near 55 km. This illustrates, as discussed above, the inward moving rainbands as cyclones intensify. Moreover, the coldest mean 85V GHz TB's (as low as 207 K) occurred for the most intense storms in the left 27.5 km box. This seems to support Burpee and Black's (1989) discussion of increasing rain rates within a decreasing radius.

It is interesting to note that the left sides of the cyclones always seem to portray the lowest TB values (the y-axis in Fig. 5.25 contains all positive numbers). This may be related to the fact that environmental air flows inward around the left side of a cyclone (with respect to direction of

MEAN TB ANOMALY vs RADIUS

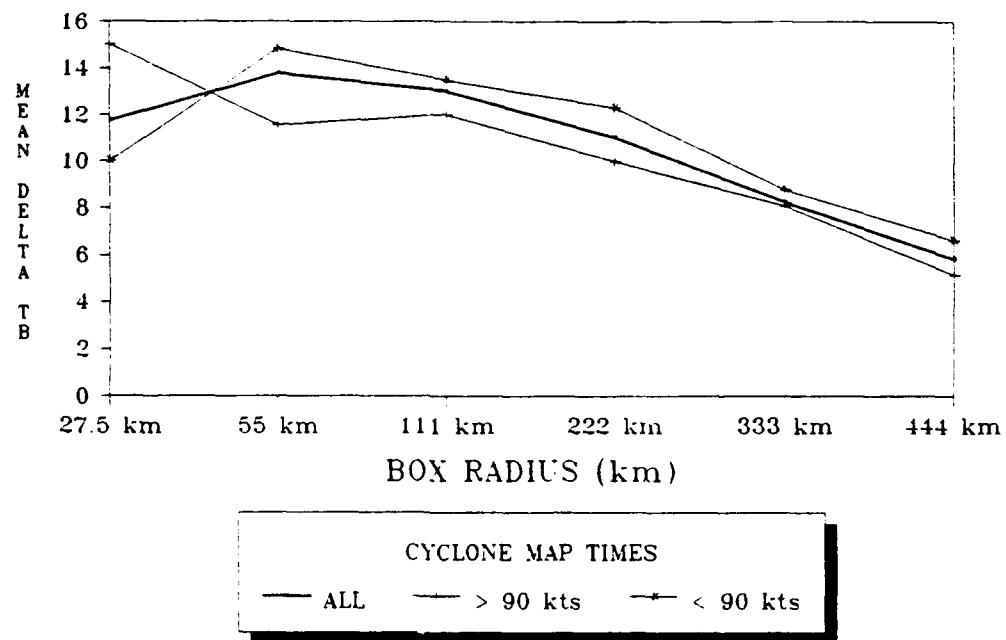


Fig. 5.25. Illustrating relationship between radius (km) from center of cyclone and mean delta TB (right-left anomaly).

motion). Similar "left-side" phenomenon were evident in the case study of Typhoon Lynn.

Also observable from Fig. 5.25 is a notable decrease in TB anomaly values beyond 111 km. This seems to support the detection of an effective radius, as mentioned earlier. It is therefore apparent that the SSM/I TB fields can portray many processes within a tropical cyclone.

d. *Lynn: a case study*

Many of the right-left anomaly phenomena can be better illustrated with a detailed look at individual storms. Typhoon Lynn offered the most map times for such an analysis, and they are shown in Table 5.2.

Figs. 5.26 through 5.30 show plots of Typhoon Lynn's lifecycle from early stages of development, through maximum intensity, to the dissipating stages of the various right-left anomalies. The 24-h central pressure plot is also shown. Except for the 27.5 km radius, the periods of intensification (the

DATE/TIME (UTC)	CURRENT INTENSITY (kts)	24hr CENTRAL PRESSURE CHANGE (mb/hr)	TRANSLATION SPEED (m/s)
17 Oct 87/2000	62	+15 (deepening)	12
18 Oct 87/0830	72	+17 (deepening)	10
19 Oct 87/0800	106	+33 (deepening)	8
21 Oct 87/2100	108	-10 (filling)	15
24 Oct 87/2200	65	-20 (filling)	4
25 Oct 87/1030	56	-7 (filling)	2
25 Oct 87/2200	45	-9 (filling)	2
26 Oct 87/1000	37	-7 (filling)	3

Table 5.2. Typhoon Lynn's lifecycle data for eight SSM/I map times.

TB ANOMALIES IN TYPHOON LYNN'S LIFECYCLE

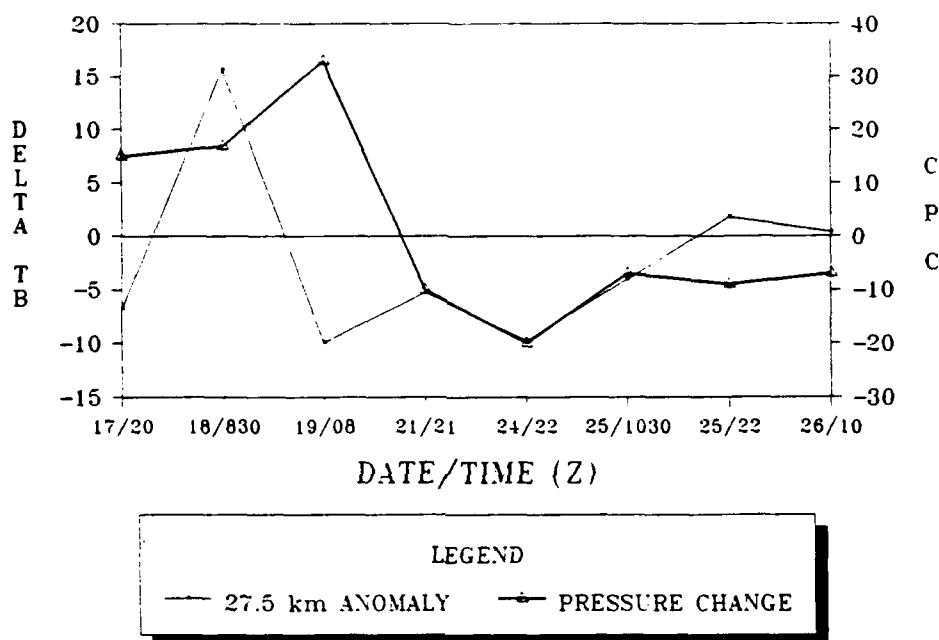


Fig. 5.26. Plot of 85 GHz vertically polarized TB anomaly, defined as the difference between the right and left 27.5 km boxes, versus time for eight map times of Typhoon Lynn. Positive numbers indicate lower mean TB values in the left box. Future (24-h) central pressure change (CPC), in mb/hr, is also shown. Positive numbers depict deepening.

TB ANOMALIES IN TYPHOON LYNN'S LIFECYCLE

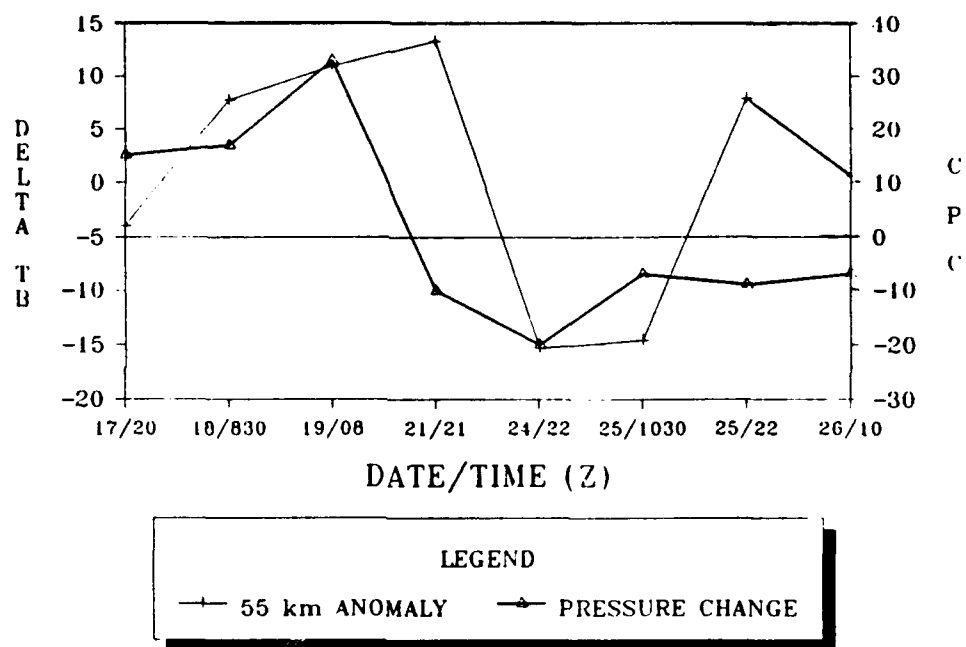


Fig. 5.27. As in Fig. 5.26, except for the 55 km case.

TB ANOMALIES IN TYPHOON LYNN'S LIFECYCLE

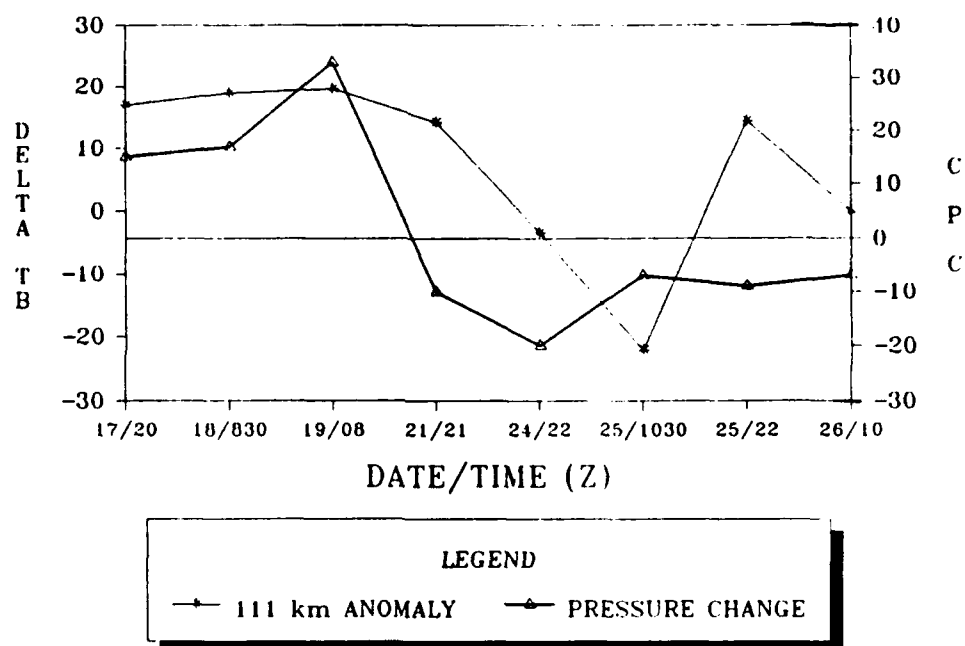


Fig. 5.28. As in Fig. 5.26, except for the 111 km case.

TB ANOMALIES IN TYPHOON LYNN'S LIFECYCLE

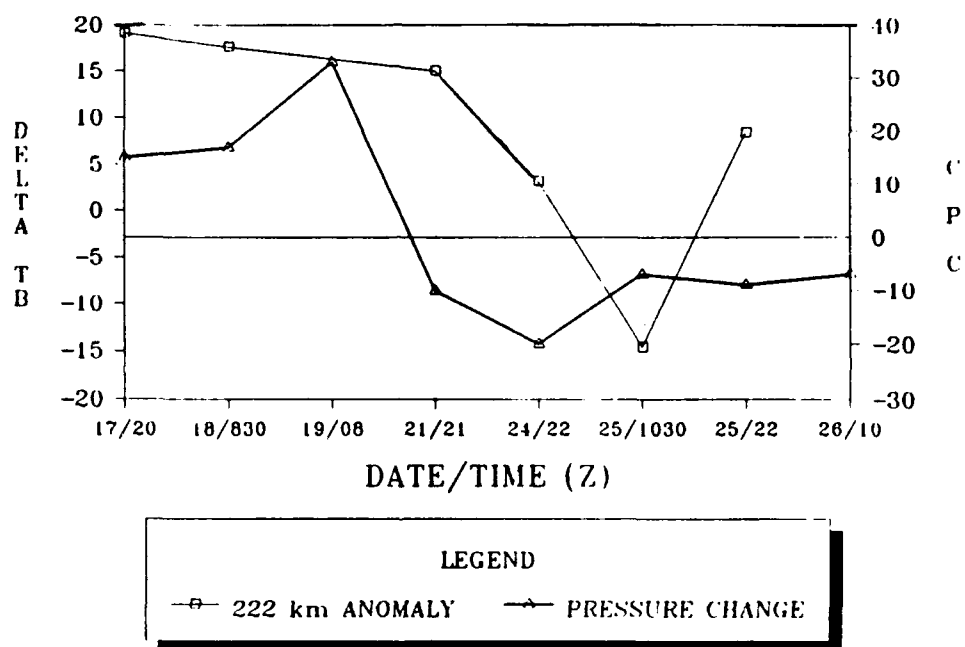


Fig. 5.29. As in Fig. 5.26, except for the 222 km case.

TB ANOMALIES IN TYPHOON LYNN'S LIFECYCLE

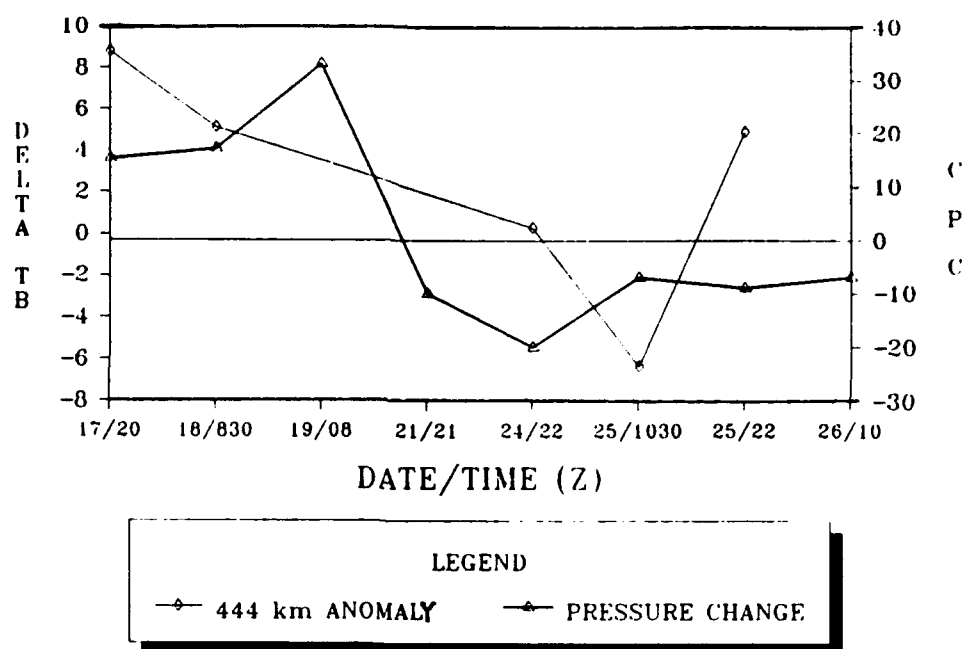


Fig. 5.30. As in Fig. 5.26, except for the 444 km case.

first three map times as shown in Table 5.2) generally show a preference for cooler TB values in the left box. After maximum intensity, the preference shifts to the right box.

The deviation of the 27.5 km radius from this pattern may indicate a changing orientation of the eyewall convection around the eye as Lynn intensified. It is also possible that since the 27.5 km box is in close proximity to the center of the storm, contamination resulted from subsidence within the eye.

It seems reasonable that the lower temperatures shifting to the right box in Figs. 5.26 through 5.30 are related to the findings of highest rain rates located in the right quadrants of moving cyclones (Shapiro, 1983 and Burpee and Black, 1989). Indeed, the maximum rain rate in Typhoon Lynn occurred near the 21 October 1987 / 2100 UTC data point.

The preference for low temperatures in the left boxes prior to maximum intensity suggests that a large rainband structure existed on the left side of

Lynn during this stage. Indeed, Lynn was a very large typhoon, and the 85V GHz data indicate that her rainbands were rotating. A fairly sudden rotation, therefore, seemed to occur near maximum intensity. This supports the findings of the outer-inner anomalies discussed earlier. Here, the 85V GHz anomaly is illustrating the changes, with intensity, in the spiral rainbands that extend outward from the eyewall region of the cyclone.

These figures also depict an increasing anomaly through maximum intensity, followed by a decrease as the storm subsides. Furthermore, Fig. 5.28 reflects an apparent band of maximum winds at 111 km, where the anomaly is the largest. The maximum rain rate occurs at the point just prior to the beginning of the anomaly's drastic sign change (except at 27.5 km). Also of interest in these figures is how the anomaly plots generally coincide with the central pressure change.

A further examination of Figs. 5.26 through 5.30 reveals the inward moving rainbands as Lynn intensifies. Fig. 5.29 shows a decrease in TB

anomaly at 222 km from the very early stages, while figs. 5.27 and 5.28 depict an increase. This reflects a movement of the spiral bands from 222 km radius inward to 111 and 55 km. Fig. 5.31 further supports this by illustrating a decrease, followed by an increase, in the minimum TB through Lynn's lifecycle. Note the radius where each minimum value occurs. These very cold TB values are reflecting the heavier convection and rainfall areas of the cyclone.

Figs. 5.32 and 5.33 depict the right-left anomaly in another fashion by examining its cross section. Fig. 5.32 shows four of Lynn's map times that occurred after maximum intensity. The top half of the chart reflects map times where the left box contained the colder TB's, while the bottom depicts map times where the right box was colder. Note the scattered distribution of the plots. Fig. 5.33 shows the same chart but for map times up to, and including, the point of maximum intensity. Note the shift of colder temperatures to the left box for all radii except 27.5 km. Also shown is the maximum anomalies occurring between 111 and 222 km.

MINIMUM TB's DURING LYNN'S LIFECYCLE

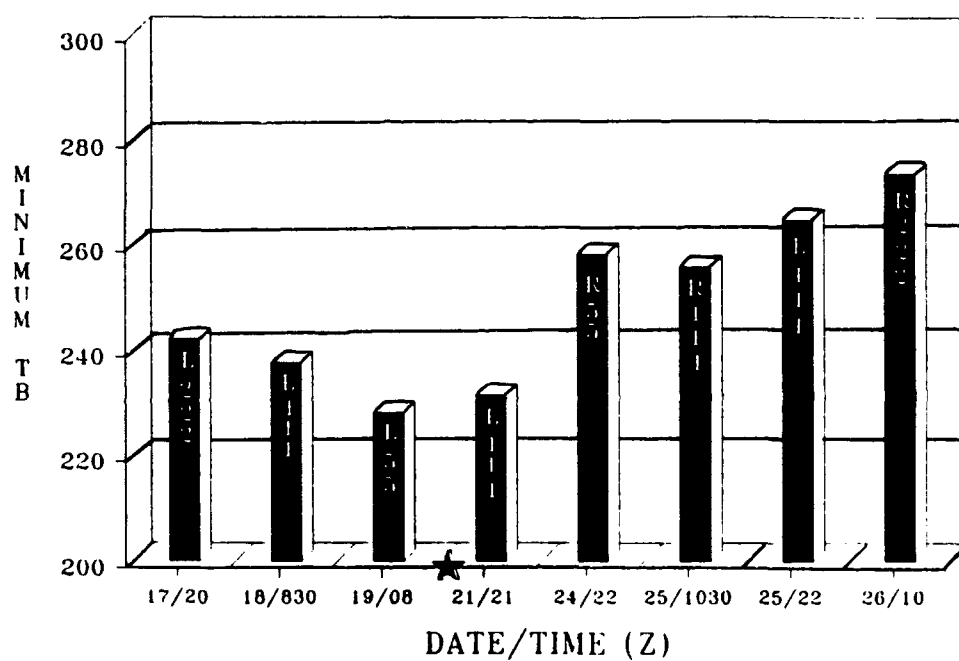


Fig. 5.31. Progression of minimum TB's during Lynn's lifecycle. The box radius containing that TB is indicated. Star portrays maximum intensity stage.

TB ANOMALIES AT VARIOUS RADII FOR TYPHOON LYNN

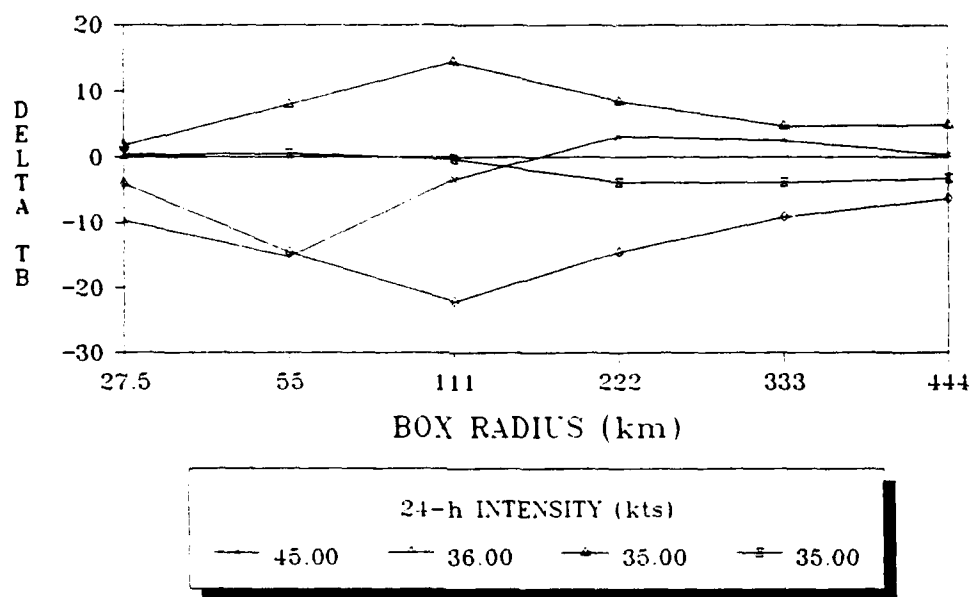


Fig. 5.32. Behavior of Lynn's TB anomalies (defined as difference between right and left box mean 85 GHz vertically polarized TB's) for all box radii. Lines shown are the map times for which future (24-h) maximum sustained winds are <50 kts. Positive delta TB values indicate lower TB's on the left side of the cyclone.

TB ANOMALIES AT VARIOUS RADII FOR TYPHOON LYNN

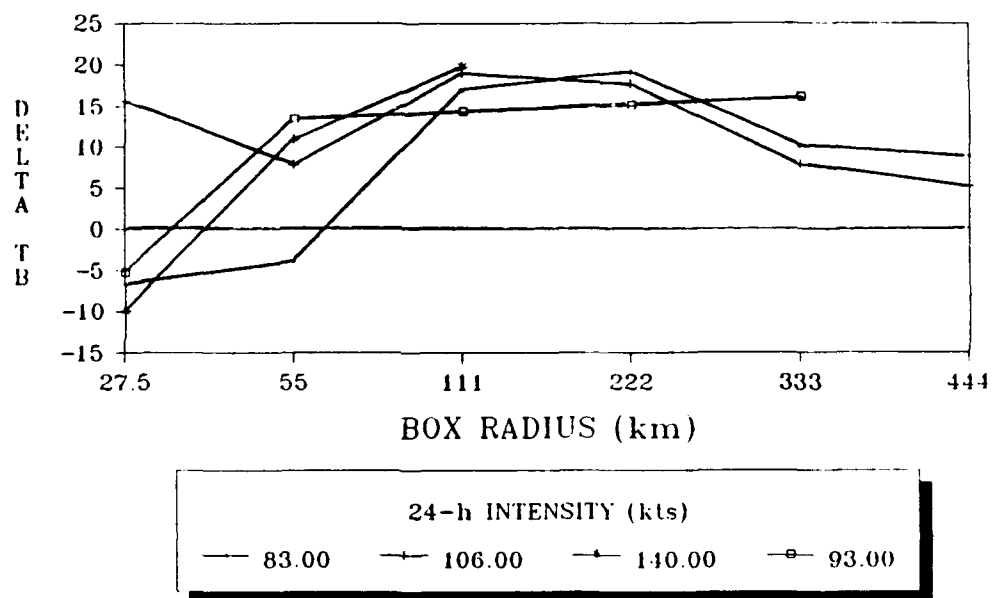


Fig. 5.33. As in Fig. 5.32, except for map times containing winds > 50 kts. Note the predominance of lower TB values in the left boxes.

An examination of typhoons Dinah and Holly revealed the same results (not shown). This supports the idea that as cyclones intensify, the 85V GHz TB anomalies can detect a certain organization of the spiral rainbands. These rainbands seem to appear closer to the eyewall on the left, then spiral outward so they are further from the eye on the right.

This phenomena is dramatically evident in the outer-inner TB anomaly of Lynn as well. Figs. 5.34 through 5.37 illustrate this for the 111 and 55 km box radii. Note the relatively close relationship between the anomaly and 24-h central pressure change in the left box, while the right box shows a large deviation. This same pattern occurred for all combinations of the TB anomaly.

The largest anomaly occurs for the 444 km annulus and 111 km inner box; illustrating once again a possible band of maximum wind at 111 km. Note, however, that the true radius of maximum wind could be somewhere between 55 and 111 km, due to the resolution of the statistical analysis. It also

TB ANOMALIES IN TYPHOON LYNN'S LIFECYCLE

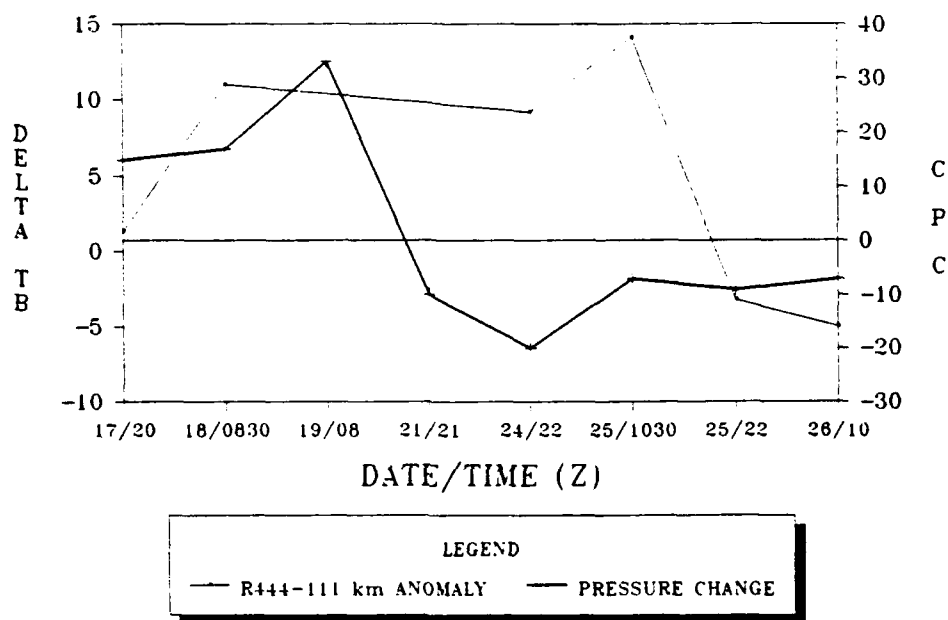


Fig. 5.34. Plot of 85 GHz vertically polarized TB anomaly (defined as the difference between mean TB in the right 444 km annulus and mean TB in the right 111 km box), versus time for eight map times of Typhoon Lynn. Future (24-h) central pressure change (CPC), in mb/hr, is also shown where positive numbers depict deepening.

TB ANOMALIES IN TYPHOON LYNN'S LIFECYCLE

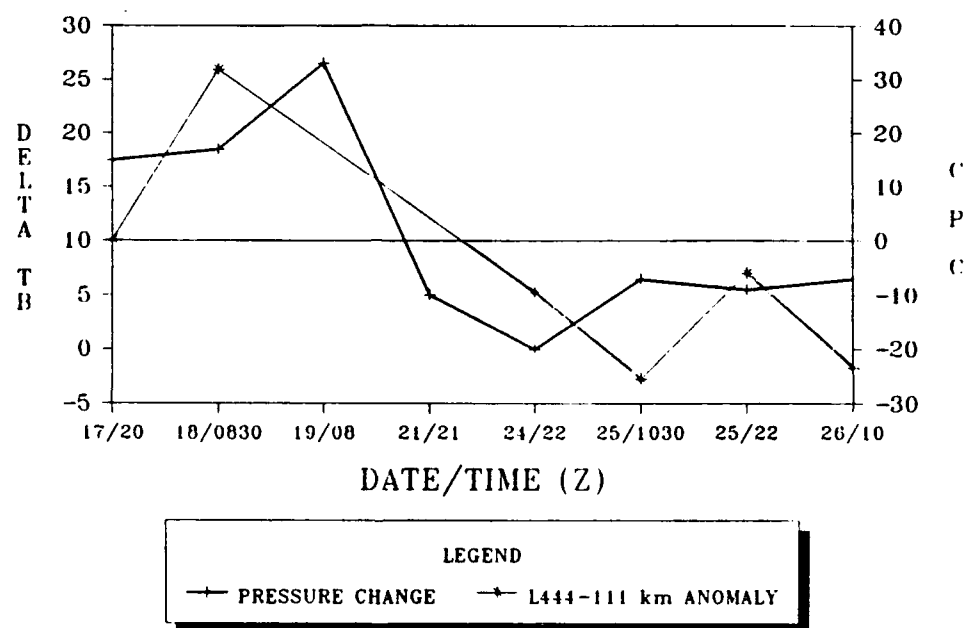


Fig. 5.35. As in Fig. 5.34, but for TB anomaly defined on the left side. Note the greater adherence of the anomaly plot to the central pressure change.

TB ANOMALIES IN TYPHOON LYNN'S LIFECYCLE

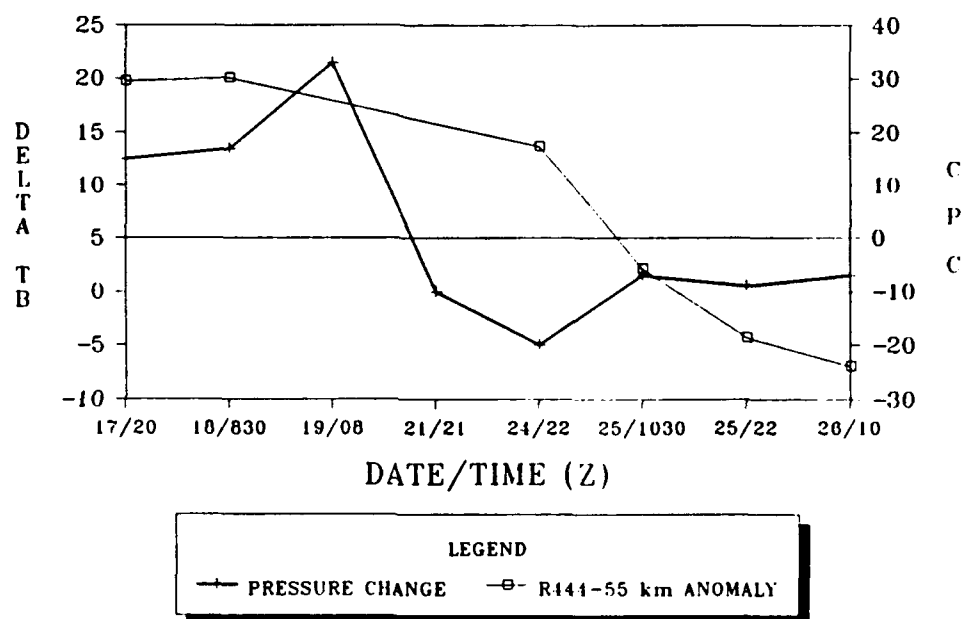


Fig. 5.36. As in Fig. 5.34, but for anomaly defined as the difference between mean TB in the right 444 km annulus and mean TB in the right 55 km box.

TB ANOMALIES IN TYPHOON LYNN'S LIFECYCLE

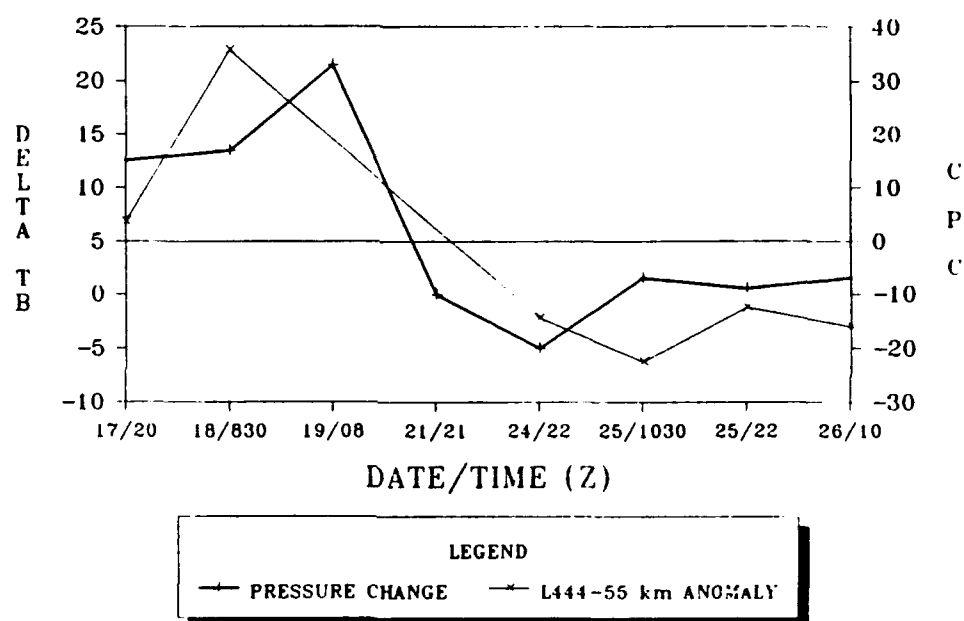


Fig. 5.37. As in Fig. 5.36, except for the left side of the cyclone.

seems reasonable that the large TB anomaly may be related to the effective radius.

Finally, a cross section of Lynn's average TB's were examined. Figs. 5.38 through 5.42 illustrate the cross section of average 85V GHz TB's for several map times. The same patterns of colder TB's residing in the left box for intensifying storms is evident here too.

Figs. 5.38, 5.39, and 5.40 depict the coldest average TB's on the left side of the cyclone, near 55 and 111 km. Fig. 5.40 (for maximum sustained winds of 108 kts) shows Lynn very near its maximum intensity. Well-defined rainbands can be seen near 111 km. It is also interesting to note the presence of a cold eye at this map time, where a warm eye was present for earlier stages.

Warm 85V GHz TB's are expected in the vicinity of the eye, due to the usually clear and non-convective environment. The cold eye present in Fig. 5.40 may be due to convective matter covering the eye, and thus sensed by the SSM/I. This seems

CROSS SECTION OF MEAN TB'S
IN TYPHOON LYNN
17 OCT 87/2000

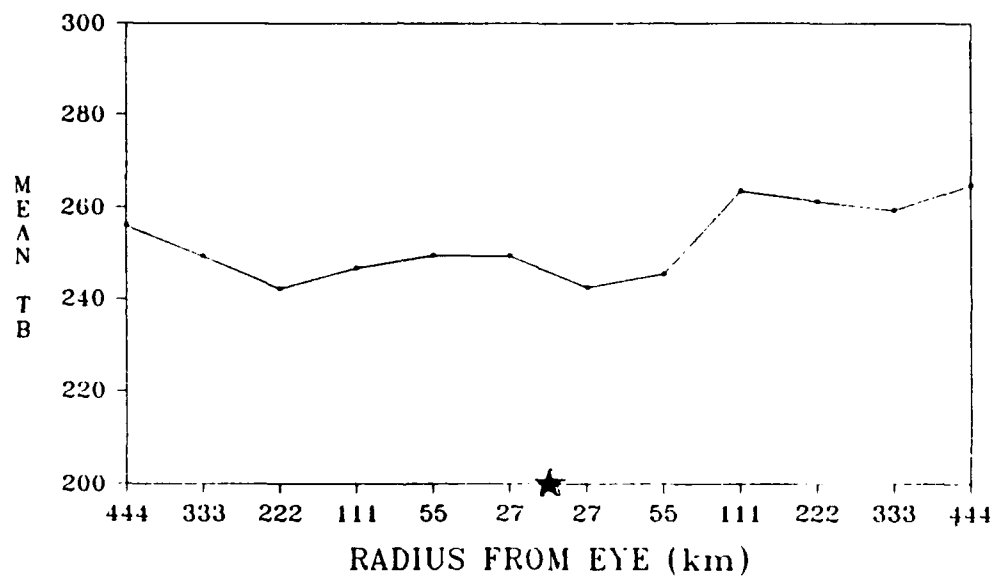


Fig. 5.38. Cross section of average 85 GHz vertically polarized Brightness Temperatures for Typhoon Lynn on 17 October 1987 at 2000 UTC (early phase). Star indicates center of storm.

CROSS SECTION OF MEAN TB's
IN TYPHOON LYNN
18 OCT 87/0830

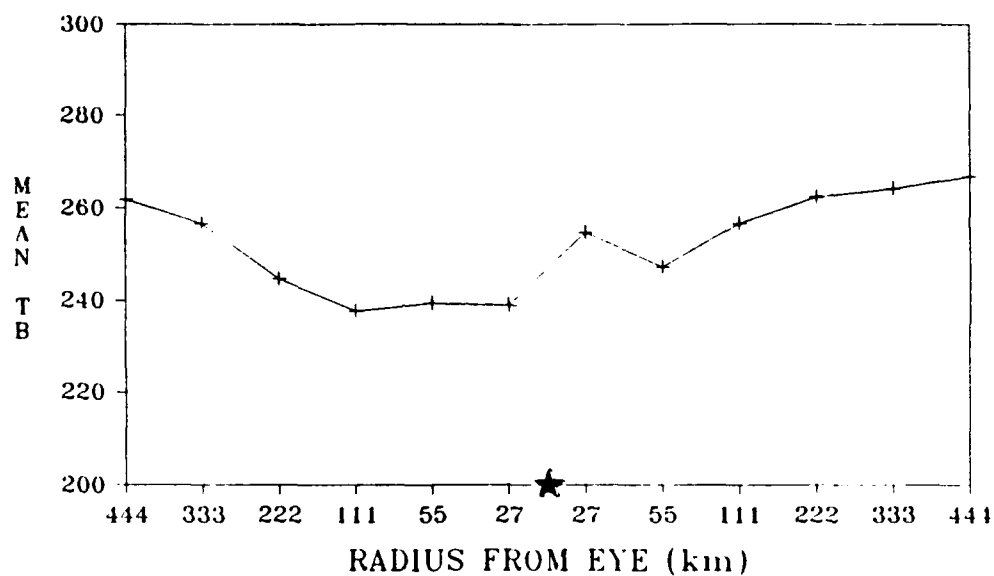


Fig. 5.39. As in Fig. 5.38, but relates to 18 October 1987 at 0830 UTC. Note the formation of cold TB eyewalls around a relatively warm eye. Also evident are lower TB values on the left side during this intensifying stage.

CROSS SECTION OF MEAN TB's
IN TYPHOON LYNN
21 OCT 87/2100

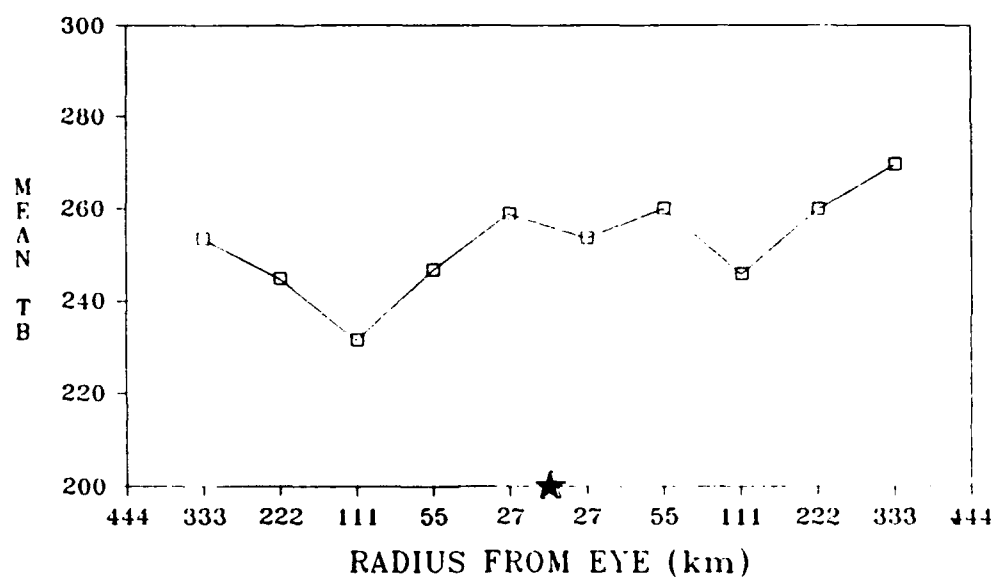
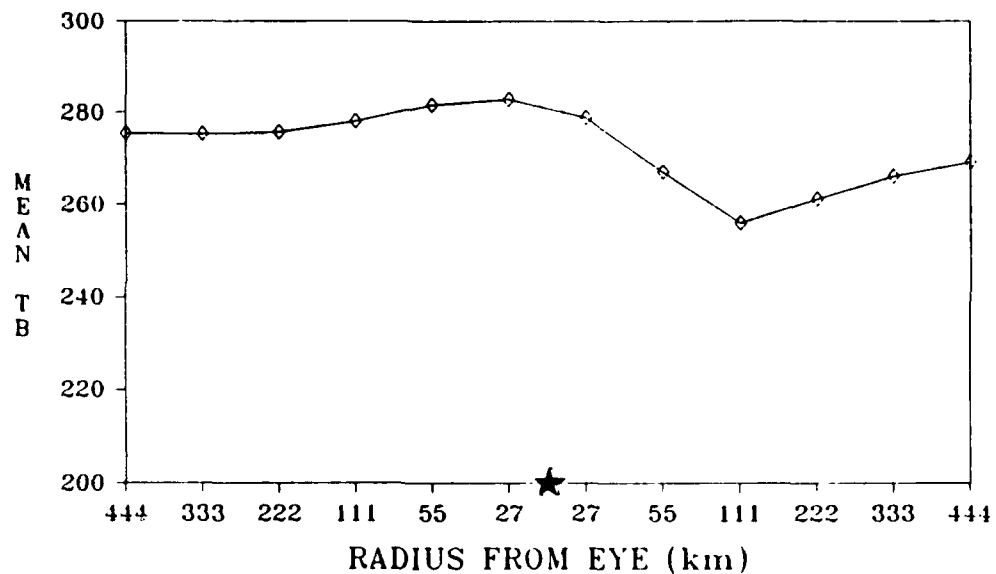


Fig. 5.40. As in Fig. 5.38, but relates to 21 October 1987 at 2100 UTC, near the time of maximum intensity. Note the development of a cold eye and well-formed eyewalls.

CROSS SECTION OF MEAN TB's
IN TYPHOON LYNN
25 OCT 87/1030



5.41. As in Fig. 5.38, but relates to 25 October 1987 at 1030 UTC, after maximum intensity. Note the shift of colder TB values to the right side.

CROSS SECTION OF MEAN TB's
IN TYPHOON LYNN
26 OCT 87/1000

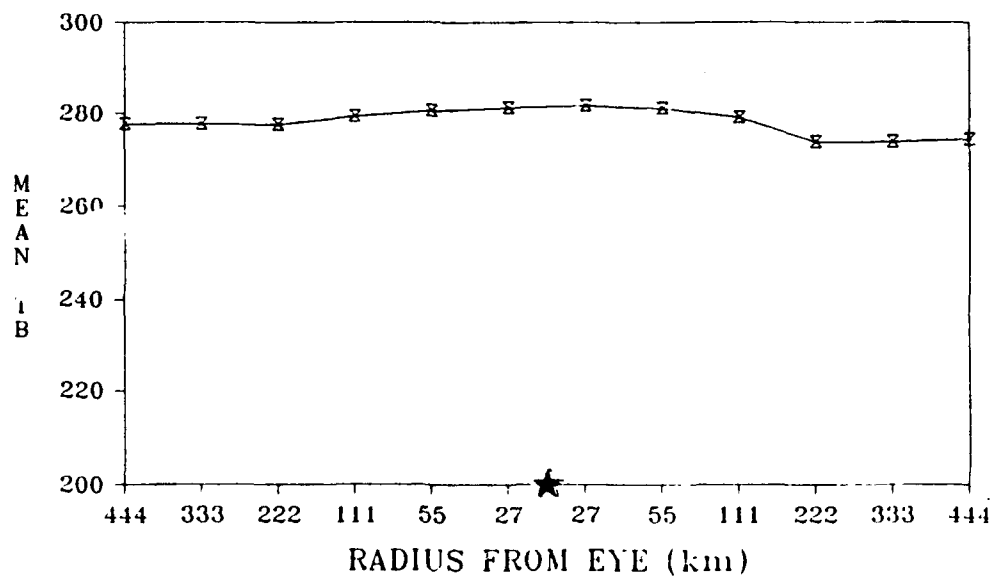


Fig. 5.42. As in Fig. 5.38, but relates to 26 October 1987 at 1000 UTC, just prior to dissipation. Note the lack of asymmetry in the TB cross section.

likely since at maximum intensity, the convective bands would be pulled inward towards the eye as discussed earlier.

Figs. 5.41 and 5.42 show the later stages of Lynn. Again, note the switch to the right of the coldest TB values, and the flattening out of the temperature plot as Lynn dissipates.

Figs. 5.43 through 5.46 depict cross sections for Lynn as defined above, but for 19H GHz. Here, opposite results to that of 85V GHz measurements can be clearly seen. Where 85V GHz showed cold mean temperatures in the vicinity of eyewalls and rainbands, 19H GHz depicts warm values. This is due to increased emission by the lower levels, including the sea surface. Also evident is the switch of the warmest (rather than coldest) TB's from left to right as described above. Lastly, the eye is depicted as cold rather than warm, due to the less emission from the lower levels in the subsidence-rich area of the cyclone eye.

CROSS SECTION OF MEAN TB's
IN TYPHOON LYNN
18 OCT 87/0830

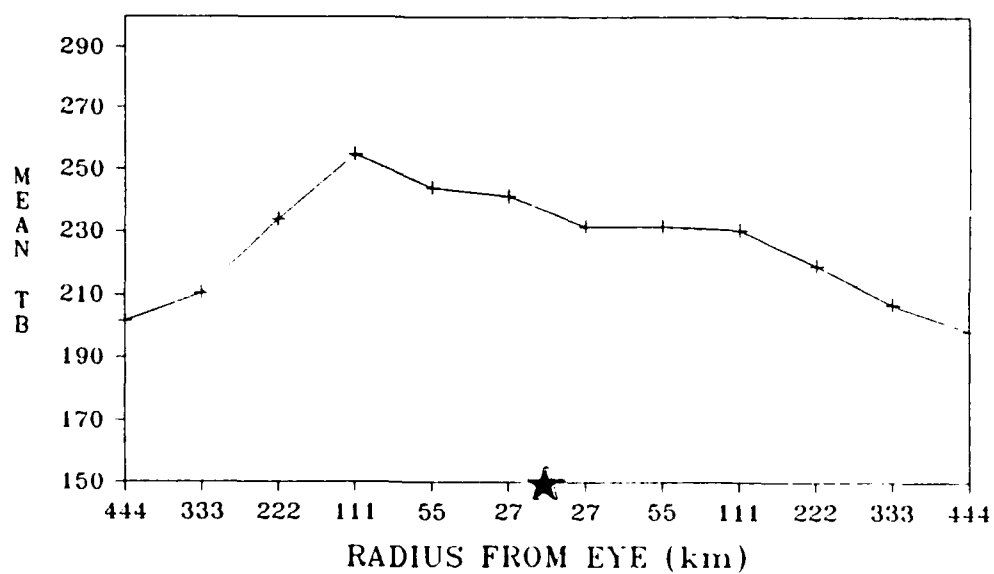


Fig. 5.43. As in Fig. 5.39, except for 19 GHz horizontal polarization. Note the inverse pattern as compared to 85V GHz.

CROSS SECTION OF MEAN TB's
IN TYPHOON LYNN
24 OCT 87/2200

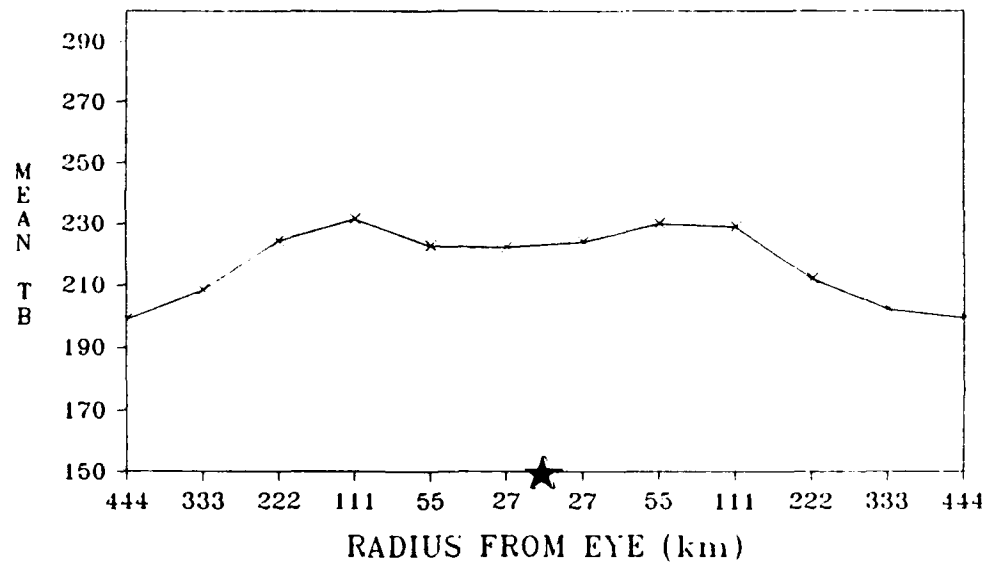


Fig. 5.44. As in Fig. 5.43, but relates to
24 October 1987 at 2200 UTC.

CROSS SECTION OF MEAN TB's
IN TYPHOON LYNN
25 OCT 87/1030

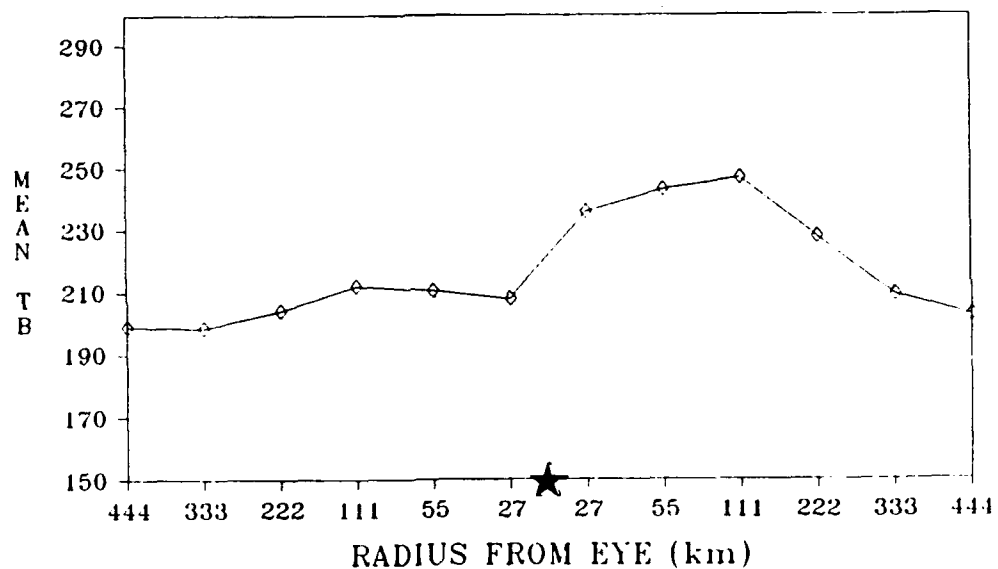


Fig. 5.45. As in Fig. 5.41, except for 19 GHz horizontal polarization. Comparison to Fig. 5.41 illustrates the opposite responses between 19H and 85V GHz.

CROSS SECTION OF MEAN TB's
IN TYPHOON LYNN
25 OCT 87/2200

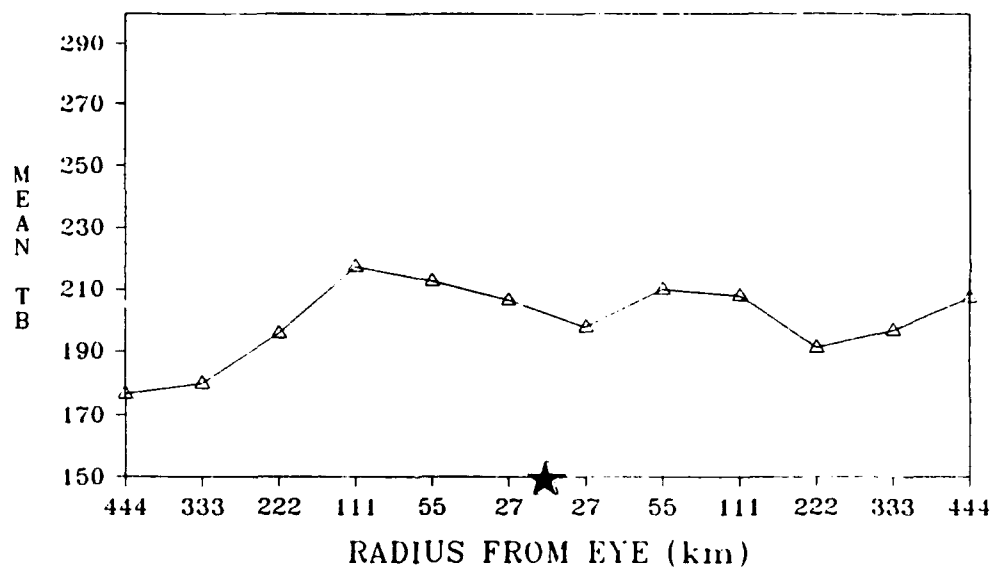


Fig. 5.46. As in Fig. 5.45, but relates to
25 October 1987 at 2200 UTC.

CHAPTER VI. CONCLUSIONS

This research undertook an automated analysis of the SSM/I TB data to find possible relationships to tropical cyclone intensity changes. It has shown that microwave emissions, particularly at the 85V GHz channel, can effectively portray important characteristics of a cyclone such as intensification and convection. Possible relationships between TB anomalies and intensification can pave the way for the use of SSM/I data in predicting tropical cyclone intensification.

Of particular interest was the capability of TB anomalies in discerning rainband position and orientation. It was shown that these anomalies would highlight asymmetries of convection in the vicinity of the eyewalls and spiral rain bands. The outer-inner type anomalies depicted the difference between the interior portions and outer environment of a cyclone. For these, the best correlations seemed to occur at the radii where the principal rainbands were located. This explained the pattern of better correlations occurring in two areas: on

the left for small interior boxes (< 111 km), and on the right for larger interior box radii. Therefore, given the delta TB within a particular radius, regression estimates similar to those shown in Chapter V could be used operationally to determine the 24-hour intensity.

It was found, however, that the best correlations (near 0.80) occurred when only storms with similar traits were considered. Therefore, through the use of several nomograms, one for each type of trait (i.e., similar directions of motion or translation speeds), fairly dependable intensity values for a 24-hour forecast period could be obtained from a given TB anomaly. Indeed, many of the scatter diagrams, including those not shown in chapter V, had similar slopes for various box radii.

As was also shown, the 85V GHz TB anomalies could portray the inward moving rain bands, and to some extent, the formation of the concentric eyewalls. This, too, could be used in an operational environment to determine the intensity changes of a typhoon, especially since the greatest

anomalies occurred near maximum intensity.

A case study of Typhoon Lynn illustrated that there was a sudden shift of cold TB's to the right half (with respect to direction of movement) at maximum intensity. Such observation could be used to determine when a typhoon has reached its peak.

Finally, it should be noted that SSM/I data must be used in conjunction with other meteorological data to obtain accurate forecasts. For example, sea surface temperatures (SST's) play an important role in the intensification and movement of a cyclone. This research could be expanded to include SST's as another stratification, as well as latitude and season. As shown in earlier research, this is important due to the complex interaction of many forces influencing tropical cyclone intensity and propagation.

APPENDIX

Definition of Terms:

- Annulus** - The area resulting from the difference between two concentric square boxes, one smaller than the other, centered on the eye of a cyclone. The thickness of such an annulus varies, depending upon the sizes of the two boxes.
- Anomaly** - The difference in mean TB between two boxes. Two types are used in this study:
- (1) outer-inner: Given two concentric square boxes sharing a common side, the mean TB from the interior box is subtracted from the mean TB of the larger. The line forming the shared box side intersects the eye, and is oriented in the direction of motion of the cyclone.
 - (2) right-left: Consider the division of a square box into two rectangular halves, so that the dividing line intersects the eye and is oriented with respect to cyclone heading. The anomaly is derived by subtracting the mean TB in the left rectangular box from the mean TB in the right.
- Box** - A rectangular area on either side of a cyclone that has one side intersecting the eye, oriented with respect to cyclone heading. The radius of the boxes vary from 27.5 km to 444 km from the center of the cyclone.
- Future Intensity** - Maximum sustained winds in kts, as determined from the Dvorak Technique (1984), 24 hours from cyclone map time.
- Map Time** - The date/time the SSM/I collected data

in orbit for a given cyclone.

- Radius** - The distance from cyclone center to the far edge of a box. Such a distance is perpendicular to the cyclone heading.
- Slow Movers** - Cyclones with a translation speed of less than 6 kts.
- TB** - Equivalent Brightness Temperature: the temperature, as measured by a radiometer, an object would have if it emitted as a blackbody.

REFERENCES

- Adler, R.F., R.A. Mack, N. Prasad, H.-Y.M. Yeh, and I.M. Hakkarinen, 1990: Aircraft microwave observations and simulations of deep convection from 18 to 183 GHz. Part I: Observations. *J. Atmos. Oceanic Technol.*, **7**, 377-391.
- Burpee, R.W., and M.L. Black, 1989: Temporal and spatial variations of rainfall near the centers of two tropical cyclones. *Mon. Wea. Rev.*, **117**, 2204-2218.
- Carr, L.E., and R.L. Elsberry, 1990: Observational evidence for predictions of tropical cyclone propagation relative to environmental steering. *J. Atmos. Sci.*, **47**, 542-546.
- Conway, R., 1989: SSM/I ascending nodal crossing data, Jun. 26, 1987 through Aug. 13, 1989. Naval Research Laboratory, Washington D.C., 173 pp.
- Dvorak, V.F., 1975: Tropical cyclone intensity analysis and forecasting from satellite imagery. *Mon. Wea. Rev.*, **103**, 420-430.
- Dvorak, V.F., 1984: Tropical cyclone intensity analysis using satellite data. NOAA Tech. Rep. NESDIS 11, Satellite Applications Laboratory, Washington, D.C., 47 pp.
- Ferraro, R.R., J.C. Alishouse, R. Scofield, W. Jiankang, and A. Timchalk, 1989: A microwave, visible, and infrared evaluation of tropical storm Floyd. Preprints. Fourth Conference on Satellite Meteorology and Oceanography, San Diego, CA., American Meteorological Society, Boston, MA., 39-44.
- Fiorino, M., and R.L. Elsberry, 1989: Some aspects of vortex structure related to tropical cyclone motion. *J. Atmos. Sci.*, **46**, 975-990.

- Gentry, R.C., E. Rodgers, J. Steranka, and W.E. Shenk, 1980: Predicting tropical cyclone intensity using satellite-measured equivalent blackbody temperatures of cloud tops. *Mon. Wea. Rev.*, **108**, 445-455.
- Glass, M., and G.W. Felde, 1989: Structure of tropical cyclones and surrounding regions as determined from OLS and SSM/I imagery analysis. Preprints. Fourth Conference on Satellite Meteorology and Oceanography, San Diego, CA., American Meteorological Society, Boston, MA., 35-38.
- , and -----, 1990: Tropical storm structure analysis using SSM/I and OLS data. Preprints. Fifth Conference on Satellite Meteorology and Oceanography, London, England, American Meteorological Society, Boston, MA., 432-437.
- Hoffman, C.W., V.G. Patterson, and D.J. McMorro, 1987: Annual Tropical Cyclone Report. NAVOCEANCOMCEN/JTWC, Guam, U.S.A., 213 pp.
- Holland, G.J., 1983: Tropical cyclone motion: environmental interaction plus a beta effect. *J. Atmos. Sci.*, **40**, 328-342.
- Holliday, C.R., and K.R. Waters, 1989: SSM/I observation of tropical cyclone gale force vicinity winds. Preprints. Fourth Conference on Satellite Meteorology and Oceanography, San Diego, CA., American Meteorological Society, Boston, MA., 267-270.
- Hollinger, J., R. Lo, G. Poe, R. Savage, and J. Peirce, 1987: Special Sensor Microwave/Imager User's Guide. Naval Research Laboratory, Washington, D.C., 178 pp.
- Lee, T.F., and A. Caughey, 1989: Images of precipitation patterns associated with tropical cyclones using the SSM/I 85 GHz channel. Preprints. Fourth Conference on Satellite Meteorology and Oceanography, San Diego, CA., American Meteorological Society, Boston, MA., 45-48.

- Liou, K.N., 1980: "An introduction to atmospheric radiation." Academic Press, San Diego.
- Merrill, R.T., 1988: Environmental influences on hurricane intensification. *J. Atmos. Sci.*, **45**, 1678-1687.
- Plante, R.J., and D.J. McMorro, 1988: Annual Tropical Cyclone Report. NAVOCEANCOMCEN/JTWC, Guam, U.S.A., 216 pp.
- Powell, M.D., 1990: Boundary layer structure and dynamics in outer hurricane rainbands. Part I: Mesoscale rainfall and kinematic structure. *Mon. Wea. Rev.*, **118**, 891-917.
- Rao, G.V., E.J. Ciardi, and D.K. Rhudy, 1989: Comparison of SSM/I rain rates and surface winds with the corresponding conventional data in the north west Pacific typhoons. Preprints. Fourth Conference on Satellite Meteorology and Oceanography, San Diego, CA., American Meteorological Society, Boston, MA., 104-107.
- , 1990: Relationship between Brightness Temperatures and typhoon intensification. Final Report. USAF-UES Summer Faculty Research Program, Geophysics Laboratory, Hanscom AFB, MA, 15 pp.
- Rhudy, D.K., 1989: Applications of microwave radiometric measurements to infer tropical cyclone intensity and strength., M.S. Thesis, St. Louis University, St. Louis, MO., available from University Microfilms, Ann Arbor, MI., 95 pp.
- Rodgers, E.B., and R.F. Adler, 1981: Tropical cyclone rainfall characteristics as determined from a satellite passive microwave radiometer. *Mon. Wea. Rev.*, **109**, 506-521.
- Shapiro, L.J., 1983: The asymmetric boundary layer flow under a translating hurricane. *J. Atmos. Sci.*, **40**, 1984-1998.

- Spencer, R.W., H.M. Goodman, and R.E. Hood, 1989: Precipitation retrieval over land and ocean with the SSM/I: Identification and characteristics of the scattering signal. *J. Atmos. Oceanic Technol.*, **6**, 254-273.
- , and R.E. Hood, 1989: SSM/I radiances correlated with 15 minute rain gauge data. Preprints. Fourth Conference on Satellite Meteorology and Oceanography, San Diego, CA., American Meteorological Society, Boston, MA., 83-85.
- , and -----, 1989: SSM/I liquid and frozen precipitation patterns in Hurricane Gilbert. Preprints. Fourth Conference on Satellite Meteorology and Oceanography, San Diego, CA., American Meteorological Society, Boston, MA., 86-89.
- Staff, Royal Observatory, 1987: Tropical Cyclones in 1987. Hong Kong, 73 pp.
- Staff, Royal Observatory, 1988: Tropical Cyclones in 1988. Hong Kong, 73 pp.
- Steranka, J., E.B. Rodgers, and R.C. Gentry, 1986: The relationship between satellite measured convective bursts and tropical cyclone intensification. *Mon. Wea. Rev.*, **114**, 1539-1546.
- Wilheit, T.T., A.T.C. Chang, J.L. King, and E.B. Rodgers, R.A. Nieman, B.M. Krupp, A.S. Milman, J.S. Stratigos, and H. Siddalingaiah, 1982: Microwave Radiometric Observations near 19.35, 92 and 183 GHz of precipitation in tropical storm Cora. *J. Appl. Meteor.*, **21**, 1137-1145.
- Willoughby, H.E., F.D. Marks, and R.J. Feinberg, 1984: Stationary and moving convective bands in hurricanes. *J. Atmos. Sci.*, **41**, 3189-3211.
- , 1988: The dynamics of the tropical cyclone core. *Aust. Met. Mag.*, **36**, 183-191.

Wu, R., and J.A. Weinman, 1984: Microwave radiances from precipitating clouds containing aspherical ice, combined phase, and liquid hydrometeors. *J. Geophys. Res.*, **89**, 7170-7178.

BIOGRAPHY OF THE AUTHOR

Jeffrey Hale McCoy was born on October 20, 1962 in Meriden, Connecticut. He was a 1980 graduate of Dundee Community High School in Carpentersville, Illinois. In 1984, he graduated from the University of Illinois at Champaign-Urbana, receiving a Bachelor of Science degree in Mathematics, and a commission as an officer in the United States Air Force. He then studied Meteorology for one year at San Jose State University, California through the Air Force Institute of Technology (AFIT). From 1985 through 1986 he served as the Wing Weather Officer for the 23rd Tactical Fighter Wing at England Air Force Base, Louisiana. In 1986 he was assigned to Halehewa Solar Observatory, Hawaii, where he was the Systems Analyst for the world-wide network of computers that control Air Force solar telescopes and disseminate data. In 1989 he returned to AFIT where he began a master's program in Meteorology at St. Louis University, Missouri. He is married to the former Tina Hextell. They have one son, Jake.